Zinc tungstate: a review on its application as heterogeneous photocatalyst

O. B. de Macedo[1,2], A. L. M. de Oliveira[1]*, I. M. G. dos Santos[1]

[1]Universidade Federal da Paraíba, Departamento de Química, NPE-LACOM, 58059-900, João Pessoa, PB, Brazil

[2]Universidade Federal da Paraíba, Programa de Pós-Graduação em Ciência e Engenharia de Materiais, João Pessoa, PB, Brazil

Abstract

$ZnWO_4$ crystallizes in a monoclinic wolframite-like structure, which has been studied for applications in heterogeneous photocatalysis for degradation, oxidation, and reduction of various contaminants. This type of tungstate has proved to be an efficient photocatalyst under both ultraviolet and visible light irradiation and, when $ZnWO_4$ forms a heterostructure with other semiconductors or when it is doped with different ions, it has a great efficiency under sunlight irradiation. For instance, the optimization of $ZnWO_4$ efficiency has been attained by its heterojunction with different semiconductors such as ZnO, one of the most used materials for this purpose, but also with other compounds such as BiOBr, $FeWO_4$, TiO_2, WO_3, Bi_2WO_6, among others. In addition, doping $ZnWO_4$ with the Ti^{4+}, Bi^{3+}, Ce^{3+}, and Co^{2+} metal ions or with nonmetals (F^- and N^{3-}) can also increase the photocatalytic yield of the material. The photocatalytic properties of $ZnWO_4$-based catalysts have been explored toward inorganic and organic molecules. However, among the variety of target molecules, organic pollutants such as methylene blue, methyl orange, and rhodamine B dyes appear as the most investigated in studies involving photocatalysis in the presence of $ZnWO_4$. In our review, we summarize important literature works, highlighting the advancement in photocatalysis using $ZnWO_4$.

Keywords: $ZnWO_4$, wolframite, heterojunction, doping, photocatalysis.

INTRODUCTION

Advanced oxidation processes (AOPs) comprise a set of techniques that under certain conditions can convert contaminants into carbon dioxide (CO_2), water, and inorganic ions as a result of oxidation reactions. Generally, the mechanism involved in AOPs is based on the generation of free radicals, especially hydroxyl radicals (•OH), which are highly reactive and have high oxidizing power [1-4]. There are many advantages attributed to AOPs, such as strong oxidizing power, the possibility of total mineralization of pollutants and possibility of total oxidation of organic species, versatility and efficiency, decomposition of oxidizer reagents innocuous to environmental products, and to be operated under standard conditions of temperature and pressure [5]. Among the variety of existing AOPs, heterogeneous photocatalysis deserves to be highlighted. This technology is constituted by a system containing more than one phase, in which a semiconductor material is present. Semiconductor acts as a photocatalyst that can promote the degradation of pollutants after being activated by exposure to UV or visible light [6, 7].

In this context, photocatalysis aims to initiate or accelerate specific redox (reduction and oxidation) reactions in the presence of irradiated photocatalysts, usually constituted by semiconductors [8, 9]. The reaction mechanisms involved in heterogenous photocatalysis are represented in Fig. 1. After absorbing light with an energy equal to or higher than the energy of the band gap, electrons are excited from the valence band (VB) to the conduction band (CB) of a semiconductor, creating electron (e^-) and hole (h^+) pairs. The h^+ in the VB is strongly oxidizing, while e in the CB is strongly reducing. The photogenerated e^-/h^+ pairs can recombine, releasing the absorbed energy in the form of heat, or migrate to the surface of the photocatalyst to promote redox reactions. When band-to-band recombination does not occur, h^+ and e^- may migrate to the surface and h^+ oxidizes an electron donor, while on the surface, the semiconductor can donate e^- to reduce an electron acceptor [7, 8, 10]. Besides the formation of the electron/hole pair, other processes are involved in heterogeneous photocatalysis, such as: the transfer of reagents to the semiconductor surface and adsorption; reaction in the adsorbed phase; desorption of products; and removal of them from the interface region [10]. As a consequence, the semiconductor efficiency depends on some parameters such as the lifetime of the electron-hole pairs and the number of active sites present on the semiconductor surface [7, 8]. Although different wide band gap materials have been widely investigated in photocatalysis, mainly based on simple oxides such as TiO_2, ZnO, SnO_2, and WO_3 [11-14], great efforts are devoted to significantly boosting the photoactivity and photoenergy conversion in photocatalytic materials since the light response is still a challenge. For instance, doping and heterojunction formation have attracted

**andrel_ltm@hotmail.com*

https://orcid.org/0000-0002-7930-6234

continuous interest for showing to be excellent strategies for this purpose.

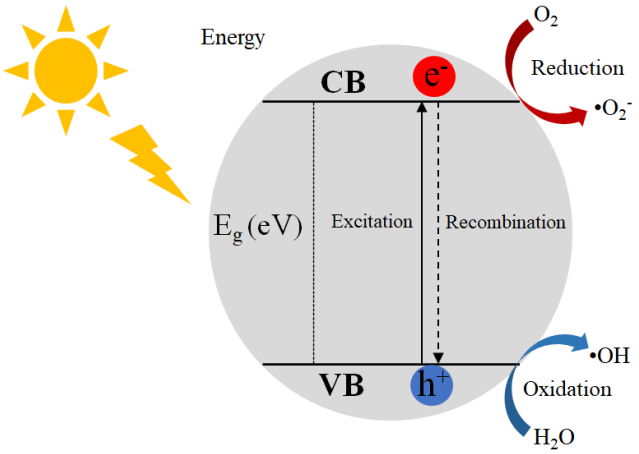

Figure 1: General mechanism of the heterogeneous photocatalysis. Photocatalyst being irradiated with a light source of an energy equal to or higher than its band gap energy.

The development of ternary metal oxides-based photocatalysts has considerably increased over the last few decades and metal tungstates have appeared as excellent alternatives for photocatalysis after the discovery of the catalytic ability of $PbWO_4$ for H_2O splitting [15]. Among the variety of metal tungstates applied in photocatalysis, zinc metal tungstate ($ZnWO_4$) is considered the most used and efficient one due to its high stability, reactivity, and versatility [16], which needs to be highlighted. $ZnWO_4$ is an important n-type semiconductor, and it presents a wide band gap energy of 3.8 eV [16-18], which may restrict its use in photocatalysis using visible light irradiation. In this context, one of the main aspects of this review work was to present an overview of the strategies employed to improve photocatalysis of $ZnWO_4$ material, such as doping and heterojunctions. In addition, we aimed to present a number of the main scientific published works concerning $ZnWO_4$-based photocatalysts. It is important to highlight that no review on the photocatalytic activity of $ZnWO_4$-based catalyst is reported yet in the literature. Thus, a comprehensive detail on the recent research progress in photocatalysis involving $ZnWO_4$ under UV, visible, and sunlight irradiation is sufficiently summarized in the present case. The mechanism of the charge transfer mechanism, formation of active species, and degradation paths involved in photocatalysis using pure and doped $ZnWO_4$ materials as well as heterostructures formed with $ZnWO_4$ are critically discussed in the review. Therefore, we believe that this review can give an important outlook for researchers studying $ZnWO_4$ and other tungstate-based material to drive new possibilities for research.

UNDERSTANDING THE INFLUENCE OF DOPING AND HETEROJUNCTIONS ON THE MATERIAL PROPERTIES

Some technologies and strategies have been developed to overcome the limitations of photoactivity of wide band gap photocatalysts under light exposure, as well as to more efficiently separate the photogenerated electron-hole pairs. Among the known strategies, metal-semiconductor and semiconductor-semiconductor heterojunctions have been demonstrated to be one of the most promising ways to prepare efficient photocatalysts. The selection of materials with different electronic band structures and band displacements improves the ability to combine and manipulate the photocatalyst behavior by the formation of heterojunctions, which offer attractive electrical and optical properties [9, 19, 20]. Heterojunctions can be defined as junctions between two intrinsically different materials sharing the same interface [21]. These heterostructures are classified into types I, II, and III as illustrated in Fig. 2. However, among these different heterostructures, type II is considered the most efficient one for charge separation, since it provides the induction of an embedded field, taking the photogenerated e^-/h^+ pairs moving toward opposite directions, in order to establish a spatial separation of electrons and holes, driven to different sides of the heterojunction.

The efficient separation of the e^-/h^+ pairs, achieved in type II heterojunction, can be further improved for the p-n type heterojunctions. This system is formed by the junction of a p-type semiconductor, in which holes are the major charge carriers, and an n-type semiconductor, in which electrons are the major carriers. For these heterojunctions, the ability

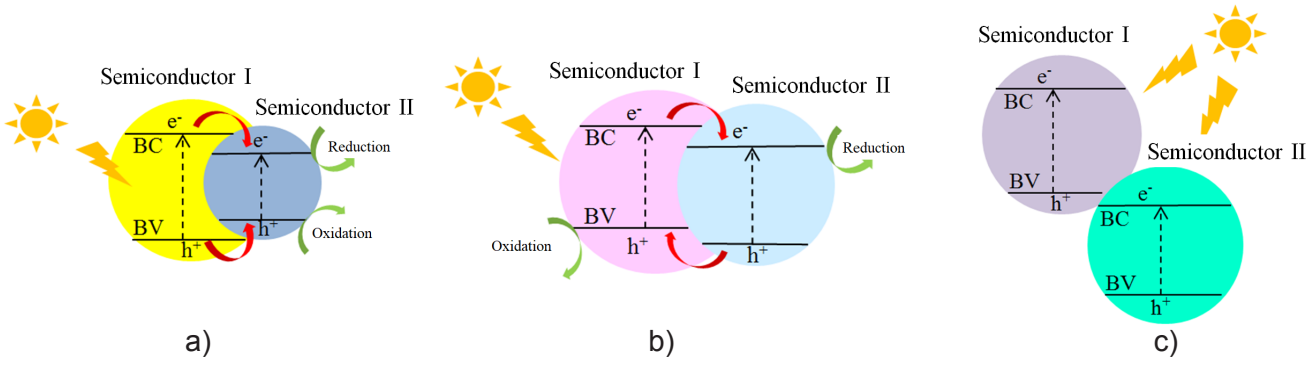

Figure 2: Schematization of the valence band (VB) and conduction band (CB) of the semiconductors and the mechanisms between the photogenerated charges for type I (a), II (b), and III (c) heterostructures.

to accelerate the migration of e^-/h^+ pairs is enhanced and photocatalytic performance is improved due to the creation of an additional electric field [20, 22]. In general, when n- and p-type semiconductors are in contact, a junction is formed with a spatial charge region at the interface between them due to the diffusion of electrons and holes when the material is immersed in an aqueous solution. In the presence of the electrical potential created at that interface, electrons and holes move in opposite directions [21, 23]. This effect can be better represented in Fig. 3. In addition to the n-p heterojunction, there are also the p-p ones, formed between two p-type semiconductors, and the analogous n-n heterojunctions, with two n-type semiconductors. The only difference between p-p and n-n heterojunctions is the mobility of the charge carriers, as p-p heterojunction is usually less attractive due to the lower mobility of holes when compared to electrons [24].

It is also worth emphasizing the Z-scheme type heterojunctions within type II heterostructures, which are inspired by the natural photosynthesis of plants, where CO_2 and water react to form carbohydrates and O_2 [25, 26]. This type of system shows significant advantages over conventional type II heterojunctions, including greater efficiency in photogenerated charge separation and higher redox potential at different active sites [27]. The Z-scheme comprises three different configurations: traditional Z-scheme, all-solid-state Z-scheme, and direct Z-scheme [28] as depicted in Fig. 4. In the traditional Z-scheme, two different photocatalysts with different oxidation/reduction abilities are combined using an appropriate redox mediator and the charge separation mechanism can be illustrated as shown in Fig. 4a. The photocatalyst with strong oxidation ability presents low VB edge position, while the one with strong reduction capacity generally has high CB edge position. Semiconductors I and II are not placed in physical contact and, during the catalytic reactions, electrons migrate from CB of photocatalyst II to VB of photocatalyst I through the electron's acceptor/donor (A/D), which is the electron mediator [21, 26, 29]. The redox reactions occurring in traditional Z-scheme heterojunction can be summarized by Eqs. A and B, where the photogenerated electrons go from the CB of photocatalyst II to the VB of photocatalyst I, through the A/D pair. When A is reduced to D by the photogenerated electrons in the CB of semiconductor II and then D is oxidized to A by holes in the VB of semiconductor I, electrons accumulate in photocatalyst I, which has the highest reduction potential, and the holes accumulate in photocatalyst II, which has the highest oxidation potential. Thus, there is a spatial separation of the e^-/h^+ pairs and a

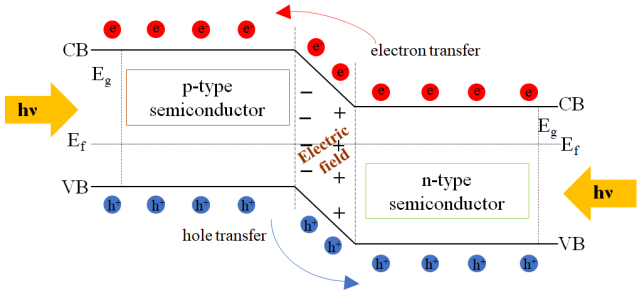

Figure 3: Schematic representation of the charge separation in n-p heterojunctions, immersed in an aqueous solution under the influence of an internal electric field (adapted from [9]).

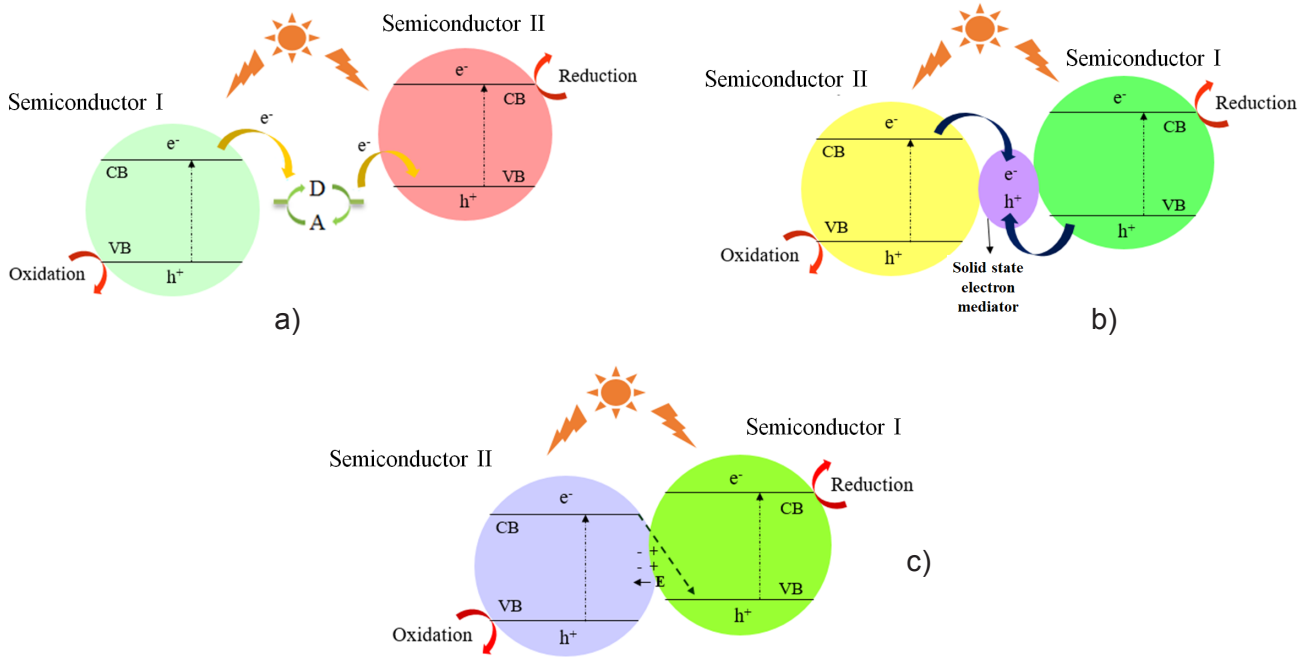

Figure 4: Mechanism of charge transfer/separation in traditional Z-scheme (with a mediator) (a), all-solid-state Z-scheme (b), and direct Z-scheme (c) photocatalytic systems.

greater redox capacity [20, 21, 29]. Perhaps the most serious disadvantage of this system is the existence of reverse reactions due to the presence of reversible mediators such as I^-/IO_3^- and Fe^{2+}/Fe^{3+} along with its applicability only in the liquid phase [28, 30].

$$A + e^- \rightarrow D \quad (A)$$

$$D + h^+ \rightarrow A \quad (B)$$

With respect to the all-solid-state Z-scheme (Fig. 4b), a solid-state conductor is employed as an electron mediator, usually noble metal nanoparticles or metal-free carbonaceous materials that make photocatalysis more effective due to its strong photoabsorption capacity. In this case, the charge transfer/separation mechanisms consist of the insertion of a conductor between semiconductors II and I, forming an ohmic contact with low contact resistance [29]. Photogenerated electrons from CB of semiconductor II may recombine with photogenerated holes from VB of semiconductor I through the ohmic contact, reducing the electron transfer of the Z-scheme. Furthermore, due to the absence of A/D pairs like in the traditional Z-scheme, reverse reactions are avoided. Thus, photogenerated holes from VB of semiconductor II and electrons from the CB of semiconductor I can directly participate in the redox reactions [28, 29]. Conversely, the direct Z-scheme has emerged as a great alternative to overcome the shortcomings of traditional and all-solid-state Z-schemes as these two configurations depend on the mediators for the charge transfer to occur. The configuration in direct Z-scheme (Fig. 4c) based photocatalyst is similar to the type II heterojunction photocatalyst, however, charge transfer mechanisms are different. In the direct Z-scheme, no mediators like redox pairs or conductors are used. The mechanism is based on two semiconductors in direct contact as illustrated in Fig. 4c. In this system, the migration path of the charge carriers is like the letter 'Z', in which the photogenerated electrons with a weak-reducing capacity of the semiconductor II recombine with the photogenerated holes with a weak-oxidizing capacity of the semiconductor I. Therefore, photogenerated electrons in semiconductor I with a strong-reducing ability and photogenerated holes in semiconductor II with strong-oxidizing capacity can be maintained. This mechanism results in a greater redox capacity of the photocatalyst, as the reverse reactions can be significantly suppressed due to the absence of redox mediators and by the reduced shielding effect created by the charge carrier mediators. In addition, the migration of the charge carriers in direct Z-scheme photocatalysts is favorable when compared to photocatalysis with heterostructures with type II configuration since the migration of photogenerated electrons from the CB of semiconductor II to the VB of semiconductor I is more feasible due to the electrostatic attraction between them [26, 28, 30, 31].

Another way to enhance the efficiency of wide band gap photocatalysts is the introduction of defects in the material crystal lattice. This strategy can affect the electronic band structure of the material, leading to important changes in its physical and chemical properties. Among the different defects, doping these semiconductors with different ions is an interesting strategy as it provides the creation of energy sublevels in the band gap region, which can be located closer to CB, if the doping impurities are electron donors, leading to n-type semiconductors. In this case, electrons are excited from the energy level created by the impurity, and no h^+ is created in the VB. However, the creation of energy bands in the band gap region may be located closer to the VB, giving origin to a p-type impurity, since this type of defect has the ability to accept an electron from the VB leaving an h^+ in its place [32-34]. In Fig. 5, it is possible to observe the modification in the electronic properties of semiconductors provided by doping with donor or acceptor impurities.

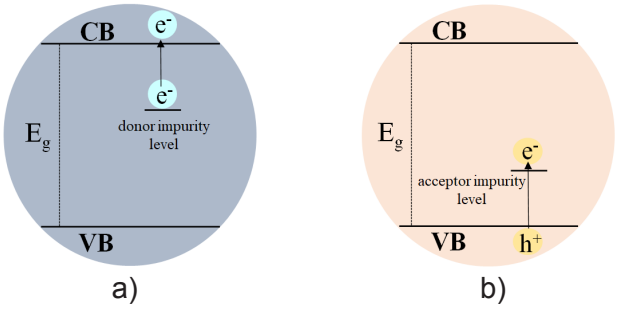

Figure 5: Electronic modifications in the band gap induced by different types of dopants: a) n-type donor; and b) p-type acceptor.

ZINC TUNGSTATE

Research concerning $ZnWO_4$-based materials applied as photocatalysts has increased over the last 20 years (especially from 2019 to 2020) as illustrated in Fig. 6. Zinc tungstate ($ZnWO_4$) belongs to the family of metallic tungstates with a high potential for application in various fields, such as photoluminescence, optical fibers, scintillating materials, humidity sensors, pigments, photocatalyst materials, among others [35-37]. Its physical and chemical properties, in terms of molecular and electronic versatility, reactivity, and stability, make $ZnWO_4$ a promising candidate in photocatalysis for the photodegradation of chemical contaminants [37-40]. At room temperature, $ZnWO_4$ has a wolframite-type structure, characterized by a monoclinic symmetry with space group *P2/c* or C^4_{2h} and no evidence of polymorphism has been reported in the literature yet for $ZnWO_4$ as it occurs in $SrWO_4$ [41], Ag_2WO_4 [42] and Fe_2WO_6 [43]. In this structure, Zn and W cations are in octahedral symmetry forming a tridimensional lattice of distorted ZnO_6 and WO_6 octahedra in alternating layers as shown in Fig. 7. Therefore, there are two minimum formula units per unit cell [40, 44].

Different synthesis routes have been employed to synthesize pure $ZnWO_4$, which include the precipitation method [45], sol-gel [46, 47], combustion method [48], conventional hydrothermal method [49], hydrothermal

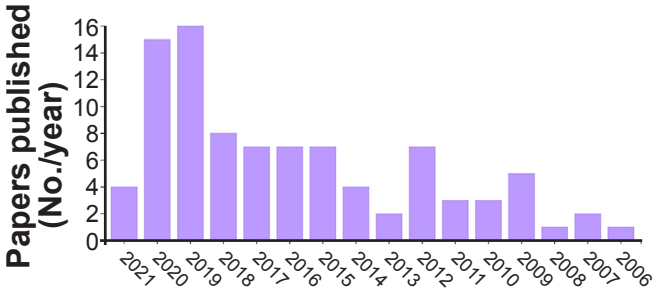

Figure 6: Number of scientific papers published per year in the period of 2006-2021 matching keywords including zinc tungstate and photocatalysis. Data collected from Web of Science.

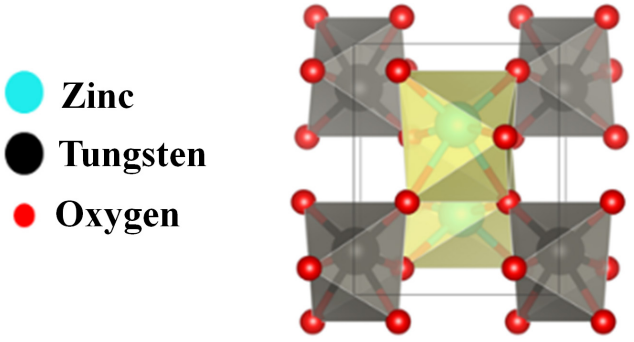

Figure 7: Crystal structure of $ZnWO_4$, showing distorted octahedra of ZnO_6 (marked in yellow color) and of WO_6 (in gray), obtained using VESTA software.

assisted microwave heating [50, 51], among others. It is known that the choice of the preparation methods may influence the morphology of the particles, surface charge characteristics, and electronic defects on the bulk and surface of the materials, and all of these may directly impact on optical properties and applications of the materials. Thus, an overview of the preparation methods of $ZnWO_4$ materials is presented to better understand the influence of those characteristics on the photocatalytic activity of $ZnWO_4$. Various researches published in the literature evaluated the photocatalytic properties of $ZnWO_4$ toward the degradation of different organic pollutants, whatever the catalyst form pure $ZnWO_4$, doped-$ZnWO_4$, or combined with other semiconductors to form heterostructures. Among the organic contaminants used to evaluate the photocatalytic efficiency of $ZnWO_4$, rhodamine B (RhB), methyl orange (MO), and methylene blue (MB) are the most used ones. Therefore, although there are other examples of works reporting photodegradation of inorganic/organic pollutant molecules, these organic dyes are highlighted throughout the manuscript.

PURE $ZnWO_4$ PHOTOCATALYST: CHARGE CARRIER MECHANISM AND EFFECT OF SYNTHESIS METHOD

As described above, $ZnWO_4$ is an n-type semiconductor with a band gap of 3.8 eV. In this mixed oxide, the majority of charge carriers are electrons. The load transfer mechanism for $ZnWO_4$ is the same as already described for a hypothetical photocatalysis mechanism in Fig. 1. The charge action mechanism occurring during photocatalysis for RhB dye degradation is described below, however, this mechanism is very similar for other organic pollutants used to evaluate the photocatalytic efficiency of pure $ZnWO_4$ in this review. It is well known that, when the energy with which the $ZnWO_4$ semiconductor is irradiated is greater than or equal to its band gap, electrons are excited from VB to CB, promoting dye degradation, once electros have a reducing action in the CB, while holes have oxidizing action in VB. These charge carriers (electron/hole pairs) migrate to the catalyst surface and react with adsorbed water and dissolved oxygen, which generate hydroxyl ($^{\bullet}OH$) and superoxide ($O_2^{\bullet-}$) radicals, later reacting with the organic pollutants, as the RhB, that are ultimately degraded into CO_2 and H_2O.

Although most photocatalysts based on semiconductor oxides are stable, low light absorption response in the visible region and the high rate of recombination of photogenerated electron/hole pairs during the process decrease the catalytic efficiency of these materials as may occur in $ZnWO_4$. In addition to the band gap value, it is necessary that the energy levels of the CB and VB are adequate for the redox potential of water, in order to produce reactive agents that facilitate the photocatalysis process. According to Wu et al. [52] the potential energy of the VB and CB, for pure $ZnWO_4$ with a band gap of 3.16 eV, is 1.784 and -1.376 eV, respectively, which can be estimated by:

$$E_{VB} = \chi - E_e + 0.5E_g \quad (C)$$

$$E_{CB} = E_{VB} - E_g \quad (D)$$

where, χ is the absolute electronegativity, which is 4.704 eV for $ZnWO_4$, E_e is the energy of free electrons at the level of the standard hydrogen electrode (approximately 4.5 eV) and E_g is the band gap. Thus, in order to improve the low visible light absorption of $ZnWO_4$, the preparation of doped-$ZnWO_4$ and $ZnWO_4$-based heterostructures has been studied by different authors and is discussed later.

Despite the disadvantage of using pure $ZnWO_4$ photocatalysis under visible light, different authors explored the activity of this material with different particle morphology under UV irradiation. Some authors explored the mechanism involved in the photocatalytic process and the role of the reactive species forming during irradiation using $ZnWO_4$. In addition, as synthesis methodology plays an important role in crystallinity, surface area, morphology, and the presence of electronic defects on the particles, these parameters also were considered by some authors and are discussed where was more adequate. For instance, Yan et al. [50] synthesized $ZnWO_4$ nanorods by microwave-assisted hydrothermal method at 140, 160, and 180 °C and evaluated the photocatalytic activity of the samples toward RhB photodegradation under UV irradiation. It is emphasized that this synthesis methodology was chosen due to its effects such as volumetric heating, higher reaction

rates, shorter reaction time, and energy-saving selectivity, besides being environmentally friendly. It was evidenced that the sample prepared at 140 °C for 5 min presented the highest photocatalytic activity, degrading about 98.01% of RhB after 6 h of reaction. The authors draw attention to the importance of the catalyst surface area; therefore, this indicates that the photocatalytic properties of $ZnWO_4$ can be significantly improved by the increase of the specific surface area, which was 25.05 and 28.10 $m^2.g^{-1}$ for samples prepared at 160 and 140 °C, respectively. Garadkar et al. [53] synthesized $ZnWO_4$ nanoparticles by coprecipitation method in a microwave-assisted heating system for applications in the photodegradation of MB and RhB dyes under UV light source (λ=254 nm). It is reported that $ZnWO_4$ degraded MB in less than 50 min and RhB in a shorter time (less than 25 min). According to the authors, the great photocatalytic activity of $ZnWO_4$ could be attributed to reduced hydrogen-related defects from hydroxyl groups adsorbed on the sample surface.

Hosseinpour-Mashkani et al. [54] reported the use of $ZnWO_4$ particles synthesized by the precipitation method using different polymeric surfactants and applied toward the photodegradation of MO dye under visible light irradiation. It was evidenced that $ZnWO_4$ nanoparticles synthesized using polyethylene glycol (PEG) as surfactant showed a higher photocatalytic efficiency, reaching 85% of MO degradation after 240 min. These authors correlated this behavior to the smallest particle size (27 nm) obtained under the mentioned conditions. In photocatalytic reactions, materials with large surface areas tend to exhibit higher photocatalytic activities, due to the greater number of active sites available for the photocatalytic reactions. It is still important to highlight that most proposed models, concerning photocatalytic mechanisms involving nanoparticles, suggest that semiconductors with high photocatalytic activity usually have a large surface area for molecule adsorption and high crystallinity to avoid electron-hole pair recombination on the surface [40, 49, 51]. According to Hosseinpour-Mashkani et al. [54], the mechanism involved in MO photodegradation can be summarized in Eqs. E to H. Under visible light, electrons (e^-) are excited from the VB to the CB of $ZnWO_4$ (Eq. E) and, simultaneously, holes (h^+) are created in VB. The h^+ in VB is captured by H_2O generating hydroxyl $^{\bullet}OH$ radicals, while e in CB reacts quickly with O_2 forming superoxide $O_2^{\bullet-}$ radicals. Both $^{\bullet}OH$ and $O_2^{\bullet-}$ radicals participate in redox reactions responsible for decomposing MO dye. The mechanism reported [54] is similar to that proposed by Altinsoy et al. [55] for the degradation of malachite green (MG) dye and by Pavithra et al. [56] for indigo carmine (IC) dye degradation. Despite the similarity among these reported studies, none of them employ an appropriate manner to investigate the mechanism of photocatalysis.

$$ZnWO_4 + h\upsilon \rightarrow ZnWO_4 + e^-_{(CB)} + h^+_{(VB)} \quad (E)$$

$$h^+ + H_2O \rightarrow {}^{\bullet}OH + H^+ \quad (F)$$

$$e^- + O_2 \rightarrow O_2^{\bullet-} \quad (G)$$

$$^{\bullet}OH + O_2^{\bullet-} + \text{methyl orange} \rightarrow \text{Degradation products} \quad (H)$$

Pereira et al. [40] synthesized $ZnWO_4$ nanocrystals by microwave-assisted hydrothermal method at three different temperatures (140, 150, and 160 ºC) and investigated the photocatalytic properties of the samples toward the degradation of RhB under UV light. The authors reported that the photocatalytic efficiency of the samples increased with the increasing synthesis temperature, reaching 100% after 40 min of irradiation for $ZnWO_4$ obtained at 160 ºC. By performing theoretical calculations within the framework of the density functional theory (DFT) and photoluminescence (PL) spectroscopy, Pereira et al. [40] also stated that crystal morphology, the type of faceted surfaces of the crystals as well as the balance of short- and medium-range structural disorder have an important effect on the photocatalytic behavior of $ZnWO_4$. In addition to that, it is proposed a photocatalytic mechanism involved in RhB dye degradation, using scavengers: $AgNO_3$ as electron (e^-) scavenger, tetrabutylammonium (TBA) as hydroxyl radical ($^{\bullet}OH$) scavenger, benzoquinone (BQ) as superoxide radical ($O_2^{\bullet-}$) scavenger and ammonium oxalate (AO) used as a hole (h^+) capturer. According to the authors, defects played a crucial role in the production of hydroxyl ($^{\bullet}OH$) and hydroperoxyl ($^{\bullet}O_2H$) radicals. They evidenced that these species are the principal involved in the $ZnWO_4$ photocatalytic degradation of RhB. Further, the top (010) surface containing vacancies associated with clusters of the type $[ZnO_4{\cdot}2V_O^x]$ is shown to be the most efficient to generate active species with higher reactivity. Reactions related to the proposed mechanism are presented in Eqs. I to L, written according to the Kroger-Vink notation and considering MO clusters (M=Zn/W) present on the surface and in the bulk of $ZnWO_4$ material. According to the authors, $[MO_x{\cdot}xV_O^{\bullet}]$ clusters are likely to be found on the surface, while $[MO_6]$' ones are mainly inside the nanocrystals.

$$[MO_6]'_{(CB)} + O_2 \rightarrow [MO_6]^x_{(CB)} + O_2' \quad (I)$$

$$[MO_x{\cdot}xV_O^{\bullet}]_{(VB)} + H_2O \rightarrow [MO_x{\cdot}xV_O^x]_{(VB)} + H^{\bullet} + HO^{\bullet} \quad (J)$$

$$O_2' + H^{\bullet} \rightarrow HO^{2\bullet} \quad (K)$$

$$HO^{\bullet} + HO^{2\bullet} + \text{RhB} + h\nu \rightarrow CCO + CO_2 + H_2O \quad (L)$$

Li et al. [49] prepared $ZnWO_4$ nanocrystals via hydrothermal reaction at temperatures up to 160 ºC and investigated the photocatalytic activity of the samples after post calcination at 700 ºC in air or oxygen atmosphere. Accordingly, the as-synthesized $ZnWO_4$ sample (via hydrothermal reaction at pH 10 and 180 ºC for 24 h) presented the highest photocatalytic behavior, with 95% of methyl orange (MO) dye degradation after 120 min under UV irradiation. The authors stated that the concentration of surface defects, such as oxygen vacancies, impacts the electron-hole recombination process. Oxygen vacancies can trap the photoinduced electron, leaving holes available for

photocatalysis to occur. As a consequence of the luminescence measurements, it was concluded that the as-synthesized $ZnWO_4$ sample presented the highest concentration of oxygen vacancies, lowest charge recombination rate by trapping electrons, and then the highest photocatalytic efficiency among the samples. Another very conventional synthesis procedure for obtaining $ZnWO_4$ particles is the combustion method. For instance, Eranjaneya and Chandrappa [48] synthesized $ZnWO_4$ nanoparticles by the combustion method, using sucrose as fuel, and the photocatalytic activity of the samples was evaluated toward the degradation of MB dye under UV irradiation. The influence of the photocatalyst amount (0.2 and 0.5 g) and MB dye concentration (5 and 10 ppm) was investigated. It was evidenced that the synthesis by combustion produced $ZnWO_4$ particles with an average size between 30-130 nm and a band gap of 3.89 eV. The photocatalytic efficiency of 0.2 g of $ZnWO_4$ using a 5 ppm MB solution was approximately 74% after 3 h under UV irradiation. The authors attributed the good photocatalytic activity of 0.2 g of the sample using 5 ppm MB concentration to the high crystallinity and large surface area (19.20 $m^2.g^{-1}$) and small particle size. Rahmani and Sedaghat [47] synthesized $ZnWO_4$ nanoparticles by sol-gel method varying pH values (pH 3, 6, and 8) and calcination temperature (400, 500, and 600 °C). The photocatalytic efficiency of $ZnWO_4$ nanoparticles was evaluated toward the degradation of MB dye under UV light irradiation. In the photocatalytic study, it was evaluated the variation in the amount of catalyst, which is, above all, a very important parameter to determine the efficiency of a photocatalyst. In this case, the variation in the concentration of $ZnWO_4$/MB dye was 1, 1.5, 2, and 3 $g.L^{-1}$. The authors observed higher photocatalytic performance for the photocatalyst calcined at 500 °C, which presented a band gap value of 3.20 eV. Regarding the photocatalytic activity of this $ZnWO_4$ photocatalyst, its efficiency increases with the increase in the amount of the catalyst for up to 2 g, and the photodegradation percentage of MB after 3 h of irradiation was 33.57%, 59.70%, 93.51% and 89.18% at photocatalyst concentration of 1, 1.5, 2 and 3 $g.L^{-1}$, respectively.

Apart from the above-mentioned methods, Neto et al. [51] reported the synthesis of $ZnWO_4$ nanoparticles by microwave-assisted hydrothermal method at 140 ºC for 5, 10, 30, 60, and 120 min and investigated the influence of the synthesis time on the adsorptive/photocatalytic properties of the samples for methylene blue (MB) and methyl orange (MO) dyes degradation. Based on the experiments, it was demonstrated that the sample synthesized at a longer hydrothermal time presented a remarkable photocatalytic result, which was correlated to the concentration of oxygen vacancies present in this sample that avoid recombination of electron/hole pairs during the process. Such behavior was previously demonstrated by Li et al. [49]. In addition to that, Neto et al. [51] provided a better insight into the mechanism involved in the photodegradation process of MB dye by the addition of radical scavengers (trapping agents) in the dye solution. For this, silver nitrate ($AgNO_3$) was used to trap e^-, ethylenediamine tetraacetate (EDTA) was employed to trap h^+, and isopropanol (IPA) was used to capture $^{\bullet}OH$. Therefore, the authors evidenced that electrons and holes have the main influence on the redox degradation of the dye. The addition of IPA showed a small reduction in photocatalytic activity of the sample, indicating hydroxyl radicals ($^{\bullet}OH$) are not the main mechanism acting in photocatalysis. This is not a very usual behavior, as most materials seem to degrade organic pollutants by an indirect photocatalysis mechanism. As evident from literature reports involving photocatalytic properties of different semiconductors as well as identification of active species by the addition of scavengers, high suppression in photodegradation of organic molecules observed by IPA addition suggest $^{\bullet}OH$ as the main species in photocatalysis. Moreover, $^{\bullet}OH$ probes have been used and confirmed the important role of these species for other semiconductors [57-63]. As the photostability and reusability of a photocatalyst are important issues for practical applications, Neto et al. [51] evaluated these factors after employing the catalysts in three consecutive photocatalytic cycles. It is important to highlight that the authors performed the tests without any heat treatment between cycles and demonstrated that the sample that presented the best discoloration capacity remained almost unchanged, with a loss of only about 2% of its efficiency after the third cycle. In addition, the authors showed that the diffractogram collected after the last cycle for the $ZnWO_4$ samples indicated the chemical stability of the material, without the presence of any secondary phase.

In recent work, Geetha et al. [64] investigated the photocatalytic properties of $ZnWO_4$ nanoparticles prepared by the coprecipitation method in the photodegradation of methylene blue (MB) dye. Geetha et al. [64] obtained $ZnWO_4$ nanoparticles with a size between 30 and 65 nm after annealing the synthesized powders at several different temperatures: 300, 400, and 500 °C for 2 h, which presented band gap values of 3.16, 3.13, and 3.11 eV, respectively. The photocatalytic behavior of the materials was evaluated under UV light irradiation with a catalyst/MB dye concentration of 0.5 $mg.mL^{-1}$ and an efficiency of 87%, 85%, and 78% for samples annealed at 300, 400, and 500 °C, respectively, was observed. It was explained that two parameters control the photocatalytic activity of $ZnWO_4$ nanoparticles, which are: crystallite size/particle size and specific surface area. According to the authors, the larger surface area or the smaller crystallite size are conductors for photocatalytic activity as they may present a large amount of surface defects, which are responsible for dye adsorption to produce photogenerated charge carriers. In addition to that, these surface defects may promote charge separation under UV light irradiation. The explanation given for the greater photocatalytic efficiency of the sample calcined at 300 °C is that this sample presented a smaller crystallite size, which is the opposite of $ZnWO_4$ calcined at 500 °C which had a larger crystallite size, leading to nanocrystals agglomeration. Similar to the studies performed by Neto et al. [51], Geetha et al. [64] identified that e^- and $^{\bullet}OH$ radicals were not the main active species formed in the process due to negligible

variation in the degradation rate constant. However, by adding acrylamide (AC) as a scavenger for capturing $O_2^{\bullet-}$, it was suggested that $^{\bullet}O_2^-$ radicals played a crucial role in the process, followed by the h^+ species.

Despite being synthesized by known conventional methods, $ZnWO_4$ was also obtained by methods not as conventional as the mechanochemical route [55] and by a new synthesis route based on the solution [65]. The preparation of $ZnWO_4$ by mechanochemical route was described by Altinsoy et al. [55] as being an effective and green method for obtaining semiconductor nanotungstate powders. The authors used for the mechanochemical treatment a grinding speed of 700 rpm for 25, 50, and 100 min using a planetary ball mill and evaluated the photocatalytic activity toward malachite green (MG) degradation under visible light. It was revealed that when the griding process time was extended to 100 min, the global particle size distribution became more homogeneous. However, the $ZnWO_4$ phase distribution with submicron size and nanoparticle size increased, while it appeared to be mechanically adhered and agglomerated among other particles by increasing process time. Regarding the band gap, the sample prepared at 700 rpm for 100 min presented a band gap value of 2.86 eV much lower than the characteristic band gap of $ZnWO_4$, which is around 3.8 eV. According to the authors, the lower band gap of the material increased its photoresponse in visible light, which is opposite to the open literature for pure $ZnWO_4$ materials, as reported by other authors. The highest photocatalytic efficiency was obtained for the sample prepared at 700 rpm for 25 min of grinding, degrading about 80% of the MG in 120 min. The authors emphasize that the combination of parameters such as crystal size, surface area, optical band gap energy, and amount of $ZnWO_4$ influenced the photocatalytic efficiency of the material.

A new synthesis solution-based method was described by Faka et al. [65]. According to the authors, this is an easy synthesis method for obtaining $ZnWO_4$ particles. The synthesis starts with a typical synthesis in solution with the formation of a yellow-green precipitate that was aged in an oven at 70 °C for 1 h. After that, the precipitate was filtrated and washed with ethanol and distilled water, so that any ions that might eventually be in the final products could be removed. Afterward, the formed powder was calcined at different temperatures of 400, 500, 600, 700, and 800 °C for 2 h to obtain pure $ZnWO_4$ nanoparticles. The photocatalytic activity of $ZnWO_4$ samples was evaluated toward the degradation of para-aminobenzoic acid under UV irradiation. Faka et al. [65] reported that the increase in the calcination temperature was accompanied by an increase in crystallite size, reaching 29.94 nm for the sample calcined at 800 °C, and this was the reason for the agglomeration/interconnection of particles. It was also reported that, in tungstates, the valence band (VB) is composed of the states related to O_{2p} and the conduction band is composed of the states related to W_{5d} and the band gap of the $ZnWO_4$ calcined at 600 °C was 3.1 eV. Regarding the photocatalytic activity, the sample annealed at 400 °C presented the lowest photocatalytic activity in the photodegradation of the para-aminobenzoic acid, reaching a degradation of 49% in 160 min under UV. It was indicated that the presence of a secondary phase in the sample calcined at 400 °C may act as recombination centers for the electron-hole pairs, decreasing the photocatalytic activity. The highest efficiency was observed, therefore, for the sample annealed at 600 °C, with degradation of 100% of para-aminobenzoic acid after 160 min of irradiation. According to the authors, the greater efficiency for this sample is because the increase in particle and crystallite size causes electron-hole migration to greater distances, avoiding recombination. Therefore, the ideal crystalline size for the samples was considered 25 nm. As a result, $ZnWO_4$ nanoparticles should be considered an efficient catalyst due to their well-ordered and homogeneous structure and morphology. Finally, the authors investigated the reusability of the catalysts after 5 consecutive photocatalytic cycles and confirmed that the samples retained a stable structure with no significant loss of activity, which indicated high stability.

The applications of $ZnWO_4$ in photocatalysis are not restricted to the degradation of organic compounds; $ZnWO_4$ was also applied for the redox conversion of heavy metals such as vanadium (V) and chromium (Cr) into V(VI) and Cr(III) cations, which have lower toxicity than the corresponding precursors. For instance, Zhao et al. [23] synthesized $ZnWO_4$ nanoparticles by hydrothermal method and investigated their photocatalytic behavior on the redox of those cations under UV irradiation (λ=365 nm). The efficiency of $ZnWO_4$ in the oxidation-reduction of V(V) and Cr(VI) reached 68.8% and 97.7%, respectively, after 180 min. The authors reported that Cr(VI) reduction increased rapidly after 120 min of irradiation, reaching stability at this time, whereas oxidation of V(V) increased continuously during the entire 180 min of the testing period so that Cr(VI) is reduced faster than V(V) is oxidized. The difference observed in the ability of $ZnWO_4$ to redox V(V) and Cr(VI) cations is due to the electrochemical redox potential of Cr(VI), which is relatively higher than that for V(V) so that the anode electrons are first consumed by the reduction of Cr(VI). Other works report the activity of $ZnWO_4$ as a photocatalyst for the degradation, oxidation, and reduction of several other compounds, as listed in Table I.

With respect to the photocatalytic activity of pure $ZnWO_4$ crystals, which concerns the charge carriers and morphology in $ZnWO_4$, Gouveia et al. [44] studied, using DFT calculations, the effect of (010), (110), (011), (001), (111), and (101) surfaces on the electronic band structure and showed an important correlation of the exposed surface with the photocatalytic mechanism in $ZnWO_4$. It was suggested that these electronic properties can be tuned as a function of the crystal morphology as also the composition of the material. As it is known, authors confirm that the charge carriers are responsible for controlling the performance of important applications in photocatalysis, since photocatalytic reactions only occur when the electrons and photoexcited holes are available on the surface. Thus, the photogenerated charge can affect conductivity and interaction with adsorbed

Table I - Summary of the works related to the application of pure $ZnWO_4$ as a photocatalyst for the degradation, oxidation, and reduction of different organic pollutants.

Catalyst type	Synthesis method	Photocatalyst concentration ($mg.mL^{-1}$)	Pollutant type	Light source	Efficiency (%)	Time (min)
$ZnWO_4$ sub-microparticles [55]	Mechanochemical	0.2	MG	Visible	83	120
$ZnWO_4$ nanoparticles [64]	Coprecipitation	1.0	MB	UV	81	180
$ZnWO_4$ nanoparticles [37]	Hydrothermal	0.5	RhB; FAD	UV	90 (RhB); 95 (FAD)	60 (RhB); 25 (FAD)
Mesoporous $ZnWO_4$ [66]	Precipitation	1.0	RhB; MG	UV	95	40
$ZnWO_4$ nanoparticles [67]	Hydrothermal	-	RhB	UV	91	60
$ZnWO_4$ nanoparticles [56]	Ionic liquid-assisted hydrothermal	0.75	IC	UV	90	120
$ZnWO_4$ nanoparticles [68]	Hydrothermal	-	C_7H_8	UV	75	55
$ZnWO_4$ nanoparticles [51]	Microwave-assisted hydrothermal	1.0	MB; MO	UV	87 (MB); 41 (MO)	120
$ZnWO_4$ nanoparticles [69]	Coprecipitation	0.2	CIP	UV	97	100
$ZnWO_4$ nanoparticles [46]	Sol-gel	0.5	RhB; FAD	UV	90 (RhB); ~100 (FAD)	180 (RhB); 60 (FAD)

MG: malachite green dye; MB: methylene blue dye; RhB: rhodamine B dye; FAD: formaldehyde; IC: indigo carmine dye; C_7H_8: toluene gas; MO: methyl orange; CIP: ciprofloxacin antibiotic.

species on the surface. Electrons can potentially promote conductivity in the material and therefore affect surface reaction mechanisms. However, charge carriers can be able to act as recombination centers, which are harmful to photoconductivity. The authors confirmed that the type of exposed surface is a key factor that defines the photoactivity of $ZnWO_4$ as they present distinct electronic band structure, impacting significantly on the redox ability of photoinduced carriers and, therefore, on the photocatalytic behavior of the prepared material. It was shown that (010) and (011) surfaces appeared to be the most reactive in $ZnWO_4$ crystals and they are composed of $[ZnO_4{\cdot}2V_O^x]$, $[WO_5{\cdot}V_O^x]$, and $[WO_6]_d$ clusters, being the oxygen vacancies the active sites for the photocatalytic process to occur.

As mentioned earlier, the defects can be not interesting in photocatalysis, since they may act as recombination centers of electron-hole pairs. However, some defects may act as mediators like oxygen vacancies (V_O^x) as suggested by Gouveia et al. [44], which is a common condition employed to improve the physicochemical properties of photocatalysts [70]. For instance, Osotsi et al. [71] synthesized non-stoichiometric $ZnWO_{4-x}$ nanorods with control of oxygen vacancies by solvothermal treatment to improve the photoresponse and photoactivity of $ZnWO_4$ and also a free-vacancy $ZnWO_4$ sample for tetracycline degradation under UV light. The authors reported that $ZnWO_4$ nanorods degraded 67% of tetracycline after 80 min under irradiation. When $ZnWO_{4-x}$ nanorods were used as a photocatalyst, an increased degradation rate was observed, reaching 91% of tetracycline degradation in 80 min. In order to understand the mechanism and the participation of the oxygen vacancies, ammonium oxalate (AO), quinone ammonium oxalate (BQ), silver nitrate ($AgNO_3$), and isopropyl alcohol (IPA) as radical scavengers were used. According to the study, $^{\bullet}OH$ radicals are not the main reactive species in the process, being $O_2^{\bullet-}$ radicals and photogenerated holes that played an important role in the entire process. Therefore, the induced defect states (V_O) are essential for the improvement of the electron transition and, therefore, of the ability of the oxygen-deficient $ZnWO_{4-x}$ nanorods to produce a greater number of photogenerated electrons in the CB to form $O_2^{\bullet-}$ radicals to efficiently degrade tetracycline in small dimensions. Simultaneously, the authors stated that photogenerated holes in the VB of the nanorods can directly oxidize tetracycline molecules.

The importance of some parameters such as particle size, catalyst, and dye concentration, has already been discussed. However, another very important parameter for photocatalysis to occur is the pH of the medium. The pH governs especially the characteristics of the catalyst surface and then the capacity of molecules to be adsorbed on the surface. Pavithra et al. [56] synthesized $ZnWO_4$ nanoparticles by the hydrothermal method assisted by ionic liquid at 180 °C for 24 h and the photocatalytic evaluation was performed using indigo carmine (IC) dye under UV light irradiation. The authors evaluated several parameters in photocatalysis of $ZnWO_4$, catalyst concentration, and dye concentration as well as solution pH. In the study, the variation in pH was performed using NaOH and H_2SO_4. Regarding the dye concentration, solutions with a

concentration of $2x10^{-5}$, $4x10^{-5}$, $6x10^{-5}$, and $8x10^{-5}$ mol.L^{-1} were prepared. It was found that the efficiency of dye degradation is inversely proportional to the dye solution concentration. This is explained by the fact that, as •OH radicals are the main ones responsible for the degradation of the dye, increasing the solution concentration the penetration of light in the solution decreases, resulting in a decrease in the amount of electrons that can reach the catalyst surface. As a result, the production of •OH radical is reduced and so is photocatalytic activity. The ideal concentration of dye in the experiment was found to be $2x10^{-5}$ mol.L^{-1} reaching 79% of dye degradation after 150 min. The catalyst concentration was also varied at 25, 50, 75, and 100 mg per 100 mL of the dye solution at $2x10^{-5}$ M, being the best results attained using 75 mg of the catalyst with 90% of the dye degradation after 120 min. The explanation given was that at lower dye solution concentration a greater number of active sites are created on the surface of the catalyst, which leads to the formation of photogenerated holes and •OH radicals. With an increase in the concentration of the catalyst, the photocatalysis efficiency increases, resulting in rapid degradation of the dye. According to the authors, with further increasing the amount of catalyst, particle agglomeration and sedimentation may occur, leading to an increase in the turbidity and opacity of the solution and, therefore, to a decrease in the generation of •OH radicals. Finally, the pH assessment was evaluated at pH values of 2, 4, 6, 9, and 12. For this evaluation, the concentration of dye at $2x10^{-5}$ M and the amount of the catalyst at 75 mg were fixed. According to the authors, the formation of •OH radicals is the main oxidizing species, and the pH of the dye solution is the key to the photodegradation of IC occurring onto $ZnWO_4$. They observed that the maximum dye photodegradation was reached at pH 12, decreasing after that. The variations in the pH results in anion-attracting/cation-repellent, which affect the adsorption of dye molecules and their photodegradation.

As demonstrated by Neto et al. [51], an important factor in photocatalysis is the recyclability and photostability of the catalyst without losing its efficiency. Thus, Pavithra et al. [56], Osotsi et al. [71], Rahmani and Sedaghat [47], Sheng et al. [68], and many other authors also reported that after the photocatalysis process toward the degradation of different organic pollutant molecules, $ZnWO_4$ catalyst can be easily recovered and reused for new photocatalytic experiments without major losses. This certainly demonstrates the possibility of employing $ZnWO_4$ in practical devices for different photocatalytic reactions. $ZnWO_4$ can also be used for the formation of reactive oxygen species (ROS), which have an important role in the photocatalyst, as ROS contains free electrons (e^-). Among these reactive species, there is hydrogen peroxide (H_2O_2), which has a high redox potential and is an important generator of •OH radicals. Anucha et al. [72] evaluated the influence of H_2O_2 on the photocatalytic efficiency of manganese(III) phthalocyanine sensitized $ZnWO_4$ nanoparticles toward bisphenol A (BPA) photodegradation under UV light. In their experiments, the authors added 5 mM of H_2O_2 to the photocatalytic reaction system and stated that is an adequate dose of H_2O_2 that should be added in order to avoid excessive electron and •OH elimination. However, the addition of 5 mM H_2O_2 to the system resulted in about 80% of BPA removal after 4 h of irradiation against 60% of removal when only manganese(III) phthalocyanine-sensitized $ZnWO_4$ nanoparticles were in the process. The authors attributed the higher efficiency of the photocatalyst by the addition of 5 mM of H_2O_2 to the additional formation of reactive species with subsequent suppression of electron-hole charge carrier recombination.

ZINC TUNGSTATE-BASED HETEROJUNCTIONS

Besides being used in its pure form, $ZnWO_4$ has also been used in the form of heterostructures with other semiconductors or metals and doped with metals or nonmetals to reduce the recombination of charge carriers and enhance photocatalytic activity. Heterostructured photocatalysts have been prepared combining $ZnWO_4$ and other different oxide materials. Considering a type II heterostructure, zinc oxide (ZnO) is an n-type semiconductor, and it is the most used one, combined with $ZnWO_4$ (ZWO) for this purpose. For instance, Hao et al. [73] synthesized pearl necklace-like ZnO-$ZnWO_4$ heterojunctions using the precipitation method followed by calcination at 750-950 ºC and evaluated the photocatalytic activity of the samples in the photodegradation of RhB dye. The authors stated that the photocatalytic performance is strongly influenced by ZnO/$ZnWO_4$ molar ratio and calcination temperature. The best photocatalytic degradation activity was observed for the sample with 1/0.08 molar ratio calcined at 850 ºC, reaching 96% of RhB degradation under UV irradiation in 60 min. Hao et al. [73] and according to other authors [74, 75], calculated the valence band (VB) and conduction band (CB) potentials and reported that the CB band edge of ZnO is higher than that observed for $ZnWO_4$. Therefore, the photogenerated electrons easily transfer from the CB of ZnO to that of $ZnWO_4$ through the heterostructure interface, while the photoinduced holes move from the VB of $ZnWO_4$ to that of ZnO. Heterojunctions based on ZnO with $ZnWO_4$ (ZnO-$ZnWO_4$) act as an active center that prevents the rapid recombination of electron-hole pairs since the electrons accumulated in the CB of $ZnWO_4$ can be captured by O_2 to produce the superoxide radicals ($O_2^{\bullet-}$) and holes accumulated in the VB of ZnO participate in the oxidation process in contact with OH or H_2O forming reactive •OH radicals. The enhanced photoactivity observed for the heterojunction in comparison to the pristine ZnO and $ZnWO_4$ compounds was due to the reduction in the recombination of photogenerated electrons and holes in the process. In addition, reuse tests were carried out for the samples in other to evaluate the efficiency and stability of the ZnO/$ZnWO_4$ catalyst. The authors evidenced that the degradation rate of RhB remained over 90% after four cycles, which confirms the high photostability of the synthesized catalyst.

Ojha and Kim [76] synthesized heterojunctions based on ZnO/ZWO by hydrothermal method and the

photodegradation of salicylic acid (SA) was investigated under UV-visible light irradiation. It was found a degradation of almost 98% of SA after 120 min under UV light and about 65% under visible irradiation. The authors attributed the photocatalytic behavior to the good interfacial alignment of the energy levels between the two semiconductors. The lower activity of the heterostructure under visible light in comparison to the UV irradiation was justified by the lower visible range photoresponse of both ZnO and $ZnWO_4$ semiconductors which leads to a low electronic excitation rate. The effect of the pH solution on the adsorption/desorption capacity of the pollutant over the catalyst surface was also evaluated. As a result, it was observed that at pH 4, 7, 8, and 10, the photodegradation of SA gradually increased from pH 4 to 7, decreasing afterward. The authors concluded that the surface charge properties of the photocatalyst as well as of the reagent have a significant effect on the interaction and consequently on the photodegradation rate. Similarly, Carvalho et al. [77] evaluated the photocatalytic activities of ZnO:$ZnWO_4$ heterojunctions synthesized by the hydrothermal method, with ZnO:$ZnWO_4$ molar ratios of 0:1, 1:1, and 3:1. The photocatalytic behavior of the heterojunctions was investigated toward the degradation of SA, MB, caffeine (CAF) and the amiloride drug (AML) in an aqueous medium, besides the degradation of ethylene gas in a gaseous medium under UV irradiation (λ=254 nm). An amount of 10 mg of the photocatalysts was used for the photodegradation of the pollutants in an aqueous medium, and 100 mg were used in a gaseous medium. According to the authors, the heterostructures exhibited greater photocatalytic performance when compared with that of $ZnWO_4$ or ZnO individually, reaching 80% of MB dye degradation after 180 min, about 90% in caffeine oxidation after 180 min, 95% of AML degradation after 60 min, and 100% of ethylene gas degradation after 180 min. The authors attributed the observed efficiency in degradation and oxidation of different compounds to the formation of the heterojunctions, which suppresses the rapid recombination of electron-hole pairs and induce the formation of oxygen reactive species, especially hydroxyl radicals, which promote organic molecule degradation.

Besides ZnO, bismuth tungstate (Bi_2WO_6) is another important semiconductor widely used to form a heterojunction with $ZnWO_4$. For instance, He et al. [78] synthesized Bi_2WO_6/$ZnWO_4$ heterojunctions by hydrothermal method with molar ratios of 0.05, 0.10, and 0.15 of Bi_2WO_6 in relation to $ZnWO_4$, for applications in the photodegradation of RhB dye under UV light. The authors reported that 20 mg of the photocatalyst named 0.1Bi_2WO_6/$ZnWO_4$ promoted almost the complete degradation of RhB after 80 min under UV irradiation. The photocatalytic efficiency of the heterojunctions, especially the 0.1Bi_2WO_6/$ZnWO_4$, was attributed to the lower recombination rate of the electron-hole pairs, induced by the band structure alignment, as photoinduced charges have a longer time to participate in the photocatalytic reaction before recombination. On the other hand, Kumar et al. [79] synthesized the Bi_2WO_6/$ZnWO_4$ heterostructures by the modified hydrothermal method using different molar ratios of Bi_2WO_6 in relation to $ZnWO_4$ (0.1, 0.2 and 0.3) for degradation of plasmocorinth B dye solution in a concentration of 12 $mg.L^{-1}$ and the catalyst concentration of 500 $mg.L^{-1}$ under UV irradiation. The transfer and separation mechanisms of the photogenerated charge carriers are analogous to the one already mentioned. Besides the electrostatic field created from the interfacial control generated by differences in the conduction and valence bands of semiconductors, where electrons and holes flow through, creating a better charge separation and optimization of photocatalytic activity, the authors emphasize the importance of the tungsten oxidation state in $ZnWO_4$ and Bi_2WO_6 which also plays an important role in the process: W^{6+} displays a highly oxidizing nature and can be easily reduced to W^{5+}. It is reported that the presence of a donor level results in the $5d^1$ configuration of W^{5+}, between the conduction (W^{6+}) and valence (O_2^-) bands. Therefore, the presence of W^{5+} and W^{6+} in Bi_2WO_6/$ZnWO_4$, and the oxygen can further re-oxidize W^{5+} to W^{6+}, promoting an improvement of the photocatalytic activity of the heterostructure.

Similarly, Ojha and Kim [76], Carvalho et al. [77], He et al. [78], and Kumar et al. [79] reported that preparing heterojunctions at different molar ratios promotes an enhanced photocatalytic efficiency compared to $ZnWO_4$, ZnO and Bi_2WO_6 pristine materials. Therefore, the formation of different heterojunctions can substantially enhance the photocatalytic properties of these semiconductors. The charge transfer mechanisms involved in ZnO:$ZnWO_4$ heterojunctions are illustrated in Fig. 8, in agreement with Carvalho et al. [77]. Accordingly, the effective separation of photogenerated charges occurs due to the photogenerated electrons in the CB of ZnO (-0.36 eV), represented by semiconductor I in Fig. 8, which migrate to the CB of $ZnWO_4$ (0.14 eV), represented by semiconductor II, instead of returning quickly to the VB [77]. Simultaneously, photogenerated holes in the VB of $ZnWO_4$ (3.66 eV) migrate to the VB of ZnO (2.84 eV), promoting an effective spatial charge separation in the heterostructure. This mechanism was very similar to those proposed also by Ojha and Kim [76] and He et al. [78]. Other studies based on the synthesis and applications of $ZnWO_4$-based heterojunctions for photodegradation of different contaminants are listed in Table II. Li et al. [80] studied the photocatalytic properties of $ZnWO_4$ heterostructured to one of the most used oxides in photocatalysis, TiO_2. The authors synthesized TiO_2/$ZnWO_4$ by sol-gel combined with the hydrothermal method and investigated the photocatalytic efficiency in the MB dye degradation under ultraviolet irradiation, using a catalyst/dye concentration of 1 $mg.mL^{-1}$. The authors reported that the photodegradation of MB reached a maximum of 94.6% when the sample with a TiO_2:$ZnWO_4$ ratio of 1:2 was used as a photocatalyst. It was revealed that the formation of the heterojunction greatly reduces the recombination rate of electrons and holes photogenerated in the process. The charge generation and transfer mechanism are the same as described by Carvalho et al. [77].

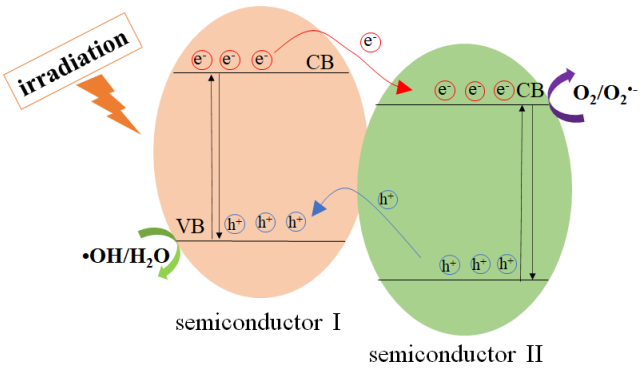

Figure 8: General mechanism for charge separation in n-n semiconductor heterostructure with different energy band-edge positions.

In a different study, heterostructures formed by $ZnWO_4$ with WO_3 have been reported by Kumar et al. [12]. The $ZnWO_4/WO_3$ heterostructures were synthesized by hydrothermal method with different WO_3 mass concentrations (0.04%, 0.08%, and 0.12%) and employed in the photocatalytic degradation of MB under visible light irradiation using a catalyst/dye concentration of 0.2 $mg.mL^{-1}$. In this work, the authors provided a study with IPA, EDTA and $AgNO_3$, used as $^{\bullet}OH$, h^+, and e^- scavengers, respectively. The efficiency in the MB photodegradation had no significant change with the introduction of $AgNO_3$ in the system, indicating that e^- were not the main active species in the reaction. However, with the introduction of IPA and EDTA, there was a reduction in the photocatalytic performance, suggesting that •OH and h^+ are the main active species and played an important role in the MB degradation process. The maximum photocatalytic efficiency was estimated at 83.6% after 2 h for $ZnWO_4$/0.12%WO_3 heterostructure. CB and VB potentials of WO_3 and $ZnWO_4$ were also calculated as described by Eqs. C and D and the estimated χ values were 3.4 and 0.74 eV for WO_3 and 3.35 and -0.15 eV for $ZnWO_4$. Thus, the charge mechanism involving $ZnWO_4$/WO_3 heterojunction was proposed. Under irradiation, both $ZnWO_4$ and WO_3 with a band gap of 3.5 and 2.7 eV, respectively, undergo photoexcitation. As the CB edge position of $ZnWO_4$ is slightly higher than the one of WO_3, electrons are transferred into the CB of WO_3. Furthermore, as the VB edge position of $ZnWO_4$ is also higher than that for WO_3, holes in the VB of WO_3 are directly transferred to the CB of $ZnWO_4$. As a result, an efficient charge separation has been achieved when this type of system is formed, which resulted in a more efficient photocatalytic. PL measurements confirmed the lower rate of charge carriers' recombination for the heterostructure compared to the pristine WO_3 and $ZnWO_4$ compounds. In addition to the studied works mentioned above, other studies involving heterojunctions of $ZnWO_4$ nanorods with metal nanoparticles, such as Ag, have been reported in the literature. Dumrongrojthanath et al. [81] decorated the surface of $ZnWO_4$ nanorods with Ag nanoparticles by sonochemical method, using different weight concentrations of Ag (1, 5, 10, and 15 wt%) in relation to $ZnWO_4$. The authors evaluated the photocatalytic efficiency of Ag/$ZnWO_4$ toward MB degradation under UV irradiation, using a catalyst/dye concentration of 1 $mg.mL^{-1}$. The heterostructures containing 10% by weight of Ag promoted the highest photocatalytic efficiency, degrading 99% of MB in 1 h. According to the findings, the degradation mechanism of MB is because the presence of heterostructured Ag nanoparticles on $ZnWO_4$ nanorods promotes the diffusion of excited electrons, resulting in an increase in the lifetime of the photogenerated charge carriers. The highest photocatalytic activity for that sample was attributed to the photoinduced electrons from the VB to the CB of $ZnWO_4$ that diffused to the Ag nanoparticles. Photoinduced electrons on Ag nanoparticles surface react with O_2 molecules adsorbed in the MB solution to produce $O_2^{\bullet-}$ radicals. The accumulation of holes may lead to the production of $^{\bullet}OH$ radicals on the catalyst surface, which were the main responsible for the decomposition of MB molecules. Thus, the photoinduced electrons in the CB of $ZnWO_4$ effectively diffused to spherical Ag nanoparticles, which inhibited the recombination process and promoted a better photocatalytic activity of the Ag/$ZnWO_4$ heterojunctions when compared to pure $ZnWO_4$ material. This process can be summarized as illustrated in Fig. 9. This same mechanism depicted in Fig. 9 was described by Li et al. [82], which also used Ag nanoparticles in the form of heterostructure with $ZnWO_4$ nanorods, synthesized by hydrothermal method using glycine as the morphology modifier. The photocatalytic behavior of the Ag/$ZnWO_4$ heterostructure in the photodegradation of MO dye under UV irradiation was studied. However, the authors emphasize that Ag reduces the number of active sites on the surface and thereby inhibits UV penetration into $ZnWO_4$ for photocatalysis to occur, therefore, an ideal Ag content is crucial for enhancing photocatalysis in Ag/$ZnWO_4$ heterostructures.

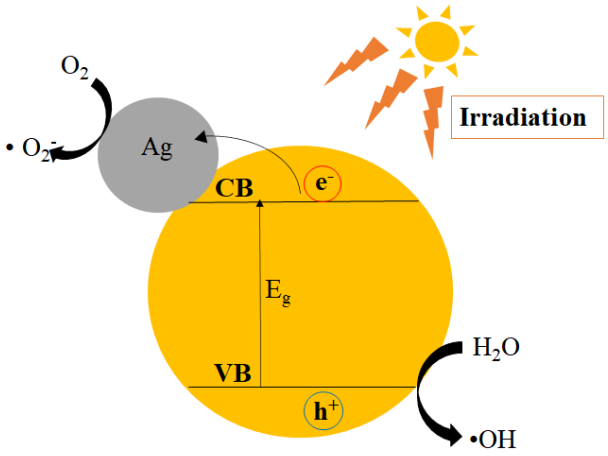

Figure 9: Charge transfer mechanism in Ag/$ZnWO_4$ heterostructure (adapted from [81]).

In addition to the compounds mentioned here, heterostructures of $ZnWO_4$ with CdS ($ZnWO_4$-CdS) have also been reported [83, 84]. Huo et al. [83] synthesized $ZnWO_4$-CdS heterojunctions formed by CdS nanoparticles distributed on $ZnWO_4$ nanorods by the hydrothermal method for ciprofloxacin (CIP) degradation under visible light irradiation. For the photocatalysis test, a 1 $mg.mL^{-1}$ concentration of catalyst/CIP was used. Wang et al. [84] also used CdS nanoparticles anchored on $ZnWO_4$ nanorods synthesized by a surface-functionalized route under moderate conditions in the presence of citric acid. The photocatalytic performance of the heterostructures was investigated in the ciprofloxacin and methylene blue dye photodegradation under visible light irradiation, using a catalyst/MB dye concentration of 0.2 $mg.mL^{-1}$ and catalyst/CIP concentration of 0.4 $mg.mL^{-1}$ [84]. Huo et al. [83] reported efficiency of about 83% for CIP photodegradation in 2 h for the $ZnWO_4$-CdS sample with a 1:1 molar ratio, while Wang et al. [84] reported that the $ZnWO_4$-CdS sample prepared with 0.1 g of citric acid, used as a ligand to build the interface of the heterojunctions between $ZnWO_4$ and CdS, showed an increase in about 6.9 times the photocatalytic activity in the photodegradation of the MB. The same sample also presented the best results for CIP degradation. In relation to the role of the charge carriers in the process, Huo et al. [83] have used IPA and $AgNO_3$ as $^{\bullet}OH$ radicals and electron (e^-) scavengers, respectively. The authors observed that the CIP degradation rates were slightly reduced and, therefore, the $^{\bullet}OH$ would be the species active in the studied process. On the other hand, Wang et al. [84] employed potassium iodide (KI), IPA and BQ used to capture h^+, $^{\bullet}OH$, and $O_2^{\bullet-}$ radicals, respectively, and they proved that h^+ and $O_2^{\bullet-}$ played irreplaceable roles in the photodegradation of MB dye.

In recent work, Alhokbany et al. [85] prepared heterostructures with $ZnWO_4$ nanoparticles on reduced graphene oxide ($ZnWO_4$-NPs@rGO) by initially synthesizing $ZnWO_4$-NP using a solvent-free method (using molten salts) heat treated at 500 ºC followed by dispersion of both $ZnWO_4$-NP and rGO in deionized water and ethylene glycol via sonication for 20 min. The authors evaluated the photocatalytic performance of the samples toward the degradation of MB dye solution under visible light (xenon lamp with 400 W and λ of ~400 nm). The catalyst/dye solution concentration was maintained at 2.5 $mg.mL^{-1}$. A degradation of ~98% dye was achieved with the use of $ZnWO_4$-NPs@rGO as a catalyst, while pure $ZnWO_4$ nanoparticles presented an efficiency of ~53% dye in 120 min. The mechanism of MB degradation using mass spectrometry equipped with an electrospray ionization source (ESI-MS) was evaluated. The degradation process of the dye could be accompanied by the transfer of electrons from the valence band (VB) to the conduction band (CB) to form the electron (e^-)/hole (h^+) pairs. The e^-/h^+ pairs generate the $O_2^{\bullet-}$ and $^{\bullet}OH$ radicals, followed by the attack on MB to oxidize it into the form of inorganic minerals (e.g., NH_4^+, H_2O, CO_2, etc.). According to the authors, the pathway photodegradation of the dye is summarized by Eqs. M to T as follows:

$$\text{Photocatalyst} + h\upsilon \rightarrow \text{Photocatalyst}(e^- + h^+) \rightarrow \text{Photocatalyst} + H^+ + {}^{\bullet}OH + O_2^{\bullet-} \quad (M)$$

$$\text{Photocatalyst}(h^+) + OH^- \rightarrow \text{Photocatalyst} + {}^{\bullet}OH \quad (N)$$

and the electrons of photocatalyst reduce the molecular O_2 to superoxide ($O_2^{\bullet-}$) at CB:

$$\text{Photocatalyst} + O_2 + e^- \rightarrow \text{Photocatalyst} + O_2^{\bullet-} \quad (O)$$

$$O_2^{\bullet-} + H^+ \rightarrow HO_2^{\bullet} \quad (P)$$

and the formation of H_2O_2 is followed by further reduction:

$$2HO_2^{\bullet-} \rightarrow H_2O_2 + O_2 \quad (Q)$$

$$H_2O_2 + e^- \rightarrow OH^- + {}^{\bullet}OH \quad (R)$$

and the degradation of hazardous methylene blue dye (MB) through direct oxidation reactions on the surface of photocatalyst gives the oxidized products:

$$^{\bullet}OH + MB \rightarrow MB^{\bullet} + H_2O \quad (S)$$

$$MB + h^+ \rightarrow MB^{+\bullet} \text{ (degraded products, i.e., } NH_4^+, H_2O, CO_2, \text{ etc.)} \quad (T)$$

With respect to the heterostructured Z-scheme photocatalysts, Reddy et al. [86] prepared a direct Z-scheme based on $NiFe_2O_4/ZnWO_4$ by depositing a different amount of one-dimensional (1D) $ZnWO_4$ nanorods (10, 20 and 30 mg) on two-dimensional (2D) $NiFe_2O_4$ nanoplates by an *in situ* hydrothermal method. The photocatalytic property of the heterostructures was evaluated in the degradation of tetracycline (TC) and rhodamine B (RhB) dye under sunlight irradiation using 0.3 $mg.mL^{-1}$ catalyst concentration. It was revealed the $NiFe_2O_4/ZnWO_4$ prepared with 20 mg of $ZnWO_4$ presented higher photocatalytic efficiency, with 98% of TC degradation after 105 min and 98% of RhB dye degradation after 70 min, with a decreased activity of about 75% for $NiFe_2O_4/ZnWO_4$ prepared with 30 mg of $ZnWO_4$. This loss in efficiency was attributed to the covering of active sites due to the large amount of $ZnWO_4$. The authors pointed out that $ZnWO_4$ deposition significantly reduces the charge recombination due to an efficient synergistic effect in the dimensionally coupled $NiFe_2O_4/ZnWO_4$ interface. By using triethanolamine (TEA), benzoquinone (BQ), and isopropyl alcohol (IPA) scavengers, the authors evidenced that $O_2^{\bullet-}$ and $^{\bullet}OH$ radicals are the main species for the photocatalysis to occur. The charge transfer mechanism proposed by Reddy et al. [86] is similar to that observed in Fig. 4c, in which the photogenerated electrons in the CB of $ZnWO_4$ (semiconductor II) flow toward the VB of $NiFe_2O_4$ (semiconductor I), recombining. The remaining h^+ in the VB of $ZnWO_4$ are positive enough to oxidize OH^- to form $^{\bullet}OH$ active species, while e^- in the CB of $NiFe_2O_4$ reduces O_2 to

$O_2^{\bullet-}$, so both species could participate in the photocatalytic reactions, effectively degrading TC and RhB molecules. The general charge transfer and the photodegradation mechanism of TC and RhB proposed for $NiFe_2O_4/ZnWO_4$ nanocomposites are summarized in Eqs. U to Y:

$$NiFe_2O_4/ZnWO_4 + h\upsilon \rightarrow NiFe_2O_4(e^-_{CB} + h^+_{VB})/ZnWO_4(e^-_{CB} + h^+_{VB}) \quad (U)$$

$$ZnWO_4(e^-_{CB}) + NiFe_2O_4(h^+_{VB}) \rightarrow ZnWO_4 + NiFe_2O_4 \quad (V)$$

$$NiFe_2O_4(e^-_{CB}) + O_2 \rightarrow O_2^{\bullet-} \quad (W)$$

$$ZnWO_4(h^+_{VB}) + H_2O \rightarrow {}^{\bullet}OH \quad (X)$$

$$O_2^{\bullet-}, {}^{\bullet}OH + TC \text{ or } RhB \rightarrow \text{Degraded products} \quad (Y)$$

Unlike Reddy et al. [86], Shan et al. [87] designed a direct binary Z-scheme $ZnWO_4$/SnS heterostructure by *in situ* deposition of SnS nanodots with various weight concentrations of 3, 6, 9, and 12 wt% on hydrothermally synthesized $ZnWO_4$ nanorods. The photocatalytic efficiency of the heterostructures was investigated toward RhB dye degradation under visible light irradiation, using a 1.67 $mg.mL^{-1}$ catalyst/dye concentration. According to the authors, $ZnWO_4$/SnS-9% presented the best photocatalytic efficiency, degrading about 97.5% of the RhB dye after 80 min. This efficiency was associated with an increased specific surface area, increased light absorption, faster interfacial charge transfer, and a more efficient charge separation rate in such heterostructure. The recyclability and reusability capacity of the catalyst were also evaluated after 4 consecutive photocatalytic runs and the authors confirmed that the samples retained a stable efficiency without significant loss of activity, indicating high stability. Finally, Shan et al. [87] investigated the role of active species involved in the photodegradation of RhB dye using scavengers, using benzoquinone (BQ), tertbutyl-alcohol (t-BuOH), and disodium ethylenediamine tetraacetate (EDTA-2Na) for the $O_2^{\bullet-}$, ${}^{\bullet}OH$ radicals and h^+ scavengers, respectively. The authors observed that the addition of BQ limited the effect of $O_2^{\bullet-}$ radicals on the RhB photodegradation, however, the addition of t-BuOH or EDTA-2Na in the reaction promoted a pronounced suppression of the RhB degradation. Thus, they concluded that the photodegradation of RhB dye occurred mainly due to ${}^{\bullet}OH$ or h^+ species.

Although binary heterojunctions are commonly found in the literature, ternary compounds-based heterostructures, which are formed by three semiconductors, have appeared to be an alternative strategy to improve the photocatalytic efficiency of $ZnWO_4$ as shown by Hamrouni et al. [88]. These authors synthesized ternary heterojunctions of SnO_2-ZnO-$ZnWO_4$ by a sol-gel method. The photocatalytic properties of these ternary heterostructures were investigated toward 4-nitrophenol degradation and partial oxidation of 4-methoxybenzyl alcohol to p-anisaldehyde under UV irradiation, using molar ratios of $0.025SnO_2$, ZnO and $0.025ZnWO_4$ that was named as $Sn_{0.025}$-Zn-$ZW_{0.025}$. The authors stated that when the ternary heterojunction is irradiated by UV irradiation, the charge separation mechanism works in such a way that the electrons generated in the CB of ZnO can be transferred to the CB of SnO_2 and $ZnWO_4$, while holes can migrate from the VB of SnO_2 and $ZnWO_4$ to the VB of ZnO. Fig. 10 represents a generic schematic model of the charge separation mechanism of a ternary diagram similar to that in SnO_2-ZnO-$ZnWO_4$. The authors also observed that the charge separation is increased and the ternary heterostructure showed to be more active than the individual oxide semiconductors. However, the photoactivity of the ternary sample was lower than that observed for binary heterostructures formed by ZnO/SnO_2 and ZnO/$ZnWO_4$ with molar ratios equal to 1/0.05. The authors justified the low photocatalytic efficiency of the ternary heterostructure due to the low activity of the ZnO/$ZnWO_4$ in relation to ZnO/SnO_2 heterojunction, leading to a reduction of the photocatalytic efficiency in the ternary sample. The ternary heterojunctions using $ZnWO_4$ are not as used as the binary ones formed with this compound.

Ternary heterostructures prepared using semiconductors and metals can also be found in the literature. For instance, Liu

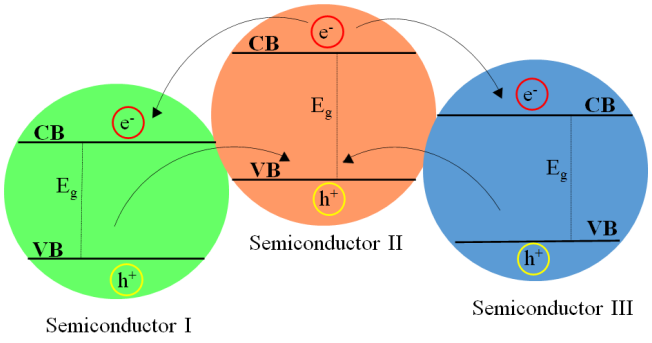

Figure 10: Charge separation mechanism in a ternary heterostructure.

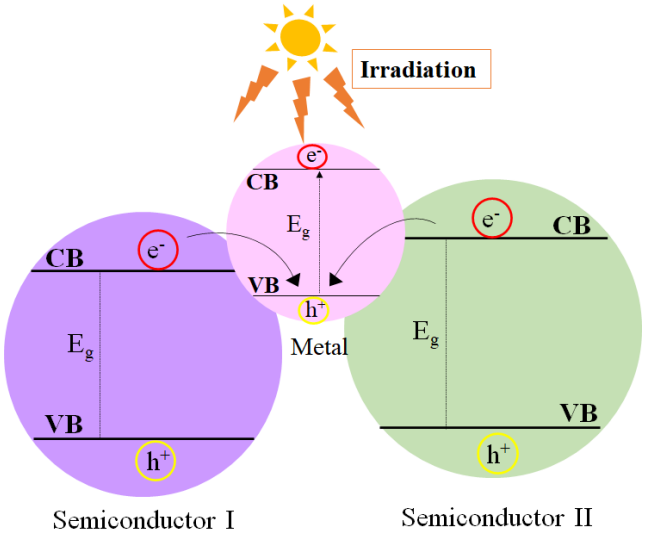

Figure 11: Mechanism of charge transfer and separation in semiconductor/metal/semiconductor heterostructure.

Table II - $ZnWO_4$-based heterostructures with different semiconductors for photodegradation of pollutants.

Heterostructure type	Synthesis method	Catalyst concentration ($mg.mL^{-1}$)	Pollutant	Light source	Efficiency (%)	Time (min)
1D/2D $BiOI/ZnWO_4$ [89]	Ultrasound treatment + precipitation	-	NO	Visible; simulated sunlight	32.32 (visible); 48.24 (sunlight)	30
$ZnWO_4$-CdS [83]	Hydrothermal	1.0	CIP	Visible	83	60
$ZnO/ZnWO_4$ [73]	Precipitation + calcination	0.83	RhB	UV	96	60
$ZnO/ZnWO_4$ [75]	Thermal plasma	1.0	CV	Sunlight	82.07	160
$ZnO/ZnWO_4$ [74]	Co-precipitation	1.0	RhB; MO; phenol	UV	96.5 (RhB); 45 (MO); 60.6 (phenol)	120
$ZnWO_4/TiO_2$ [80]	Sol-gel + hydrothermal	1.0	MB	UV	94.6	120
$Ag/Ag_2WO_4/ ZnWO_4$ [33]	Hydrothermal	-	RhB	Simulated sunlight	54.73	15
$ZnWO_4/g\text{-}C_3N_4$ [90]	Hydrothermal	0.2	RhB; 4-CP	Visible	99 (RhB); 78 (4-CP)	100
$BiOBr/ZnWO_4$ [91]	Deposition	0.5	RhB	Visible	~98	16
$g\text{-}C_3N_4\text{-}ZnWO_4$ [92]	Hydrothermal	0.5	MB; phenol	Visible	86 (MB)	150 (MB); 720 (phenol)
$Bi_2O_2CO_3/ZnWO_4$ [93]	Hydrothermal	0.5	MB	UV	95	30
$Cu_2O/ZnWO_4$ [94]	Precipitation	-	MB	Visible	90	90
$In_2S_3/ZnWO_4$ [95]	Hydrothermal	1.0	RhB	Visible	96	110
$FeWO_4$@$ZnWO_4$/ZnO; $ZnWO_4$/ZnO [17]	Hydrothermal	1.0	RhB; MB; phenol	Visible	92.3 (RhB); 66.1 (MB); 58.5 (phenol)	240 (RhB, MB), 360 (phenol)
$ZnWO_4/BiOBr$ [96]	Precipitation	1.0	TC	Visible	85.76[a]; 49.3[b]	90
LAS/ZnO/$ZnWO_4$ (LAS, schizolytic luffa sponge) [97]	Hydrothermal + mechanical force solid phase	10	RhB	UV	98	30
$ZnWO_4/Ag_3PO_4$ [98]	Precipitation	0.8	MO	Visible	95	35
$ZnWO_4$/Bi* [99]	Two-step hydrothermal-solvothermal	-	NO	Visible; simulated sunlight	11.7 (visible); 55.29 (simulated sunlight)	30
$ZnWO_4$/Ag* [82]	Photodeposition	1.0	MO	UV	99.5	80

*NO: nitric oxide; CIP: ciprofloxacin antibiotic; RhB: rhodamine B; CV: crystal violet; MO: methyl orange; MB: methylene blue; 4-CP: 4-chlorophenol; TC: tetracycline antibiotic; [a]: degradation; [b]: mineralization; *: materials classified as semiconductor/metal composites, differently to the other heterostructures presented in this table.*

et al. [33] combined Ag, Ag_2WO_4, and $ZnWO_4$ compounds to form heterojunctions with different $ZnWO_4$ molar ratios, varying from 0 to 5% of $ZnWO_4$. The photocatalytic efficiency of the different heterostructures was investigated toward RhB degradation under simulated solar irradiation. In this work, Ag^0 particles produce electrons and holes by surface plasmon resonance (SPR), under this irradiation; the photoinduced electrons from the CB of Ag_2WO_4 and $ZnWO_4$ cannot react with O_2 to produce $O_2^{\bullet-}$ due to the difference in the valence and conduction band energies (E_{VB}=2.89 eV

and E_{CB}=0.11 eV for Ag_2WO_4 vs E_{VB}=3.47 eV and E_{CB}=-0.19 eV for $ZnWO_4$), and the $O_2/O_2^{\bullet-}$ potential is -0.33 eV. In this sense, the holes formed in Ag^0 particles recombine with the photoinduced electrons of the Ag_2WO_4 and $ZnWO_4$ semiconductors and, therefore, a large number of electrons is accumulated on the surface of the Ag^0 particles. As a result, the photogenerated electrons capture O_2 and generate $O_2^{\bullet-}$, while the holes in VB of Ag_2WO_4 and $ZnWO_4$ oxidize OH^-/H_2O to generate $^{\bullet}OH$ radicals. Therefore, Ag^0 plays a significant role in the formation of $O_2^{\bullet-}$ species, accelerating the separation of photoinduced charge carriers, and providing an increase in the photocatalytic activity in $Ag/Ag_2WO_4/ZnWO_4$ heterostructure. Fig. 11 represents a hypothetical charge transfer and charge separation mechanism that occurs in one metal and two semiconductors based on ternary heterostructure.

DOPED $ZnWO_4$ PHOTOCATALYSTS

$ZnWO_4$ has an absorption range limited to the ultraviolet part of the solar spectrum, due to its wide band gap, limiting its application. Thus, studies and improvements have been carried out in order to regulate the band structure of $ZnWO_4$ to improve its photocatalytic efficiency. For this, many studies have been dedicated to the doping of $ZnWO_4$ with both metallic and nonmetallic ions as different foreign ions added into the crystal structure of the material may provide important modifications not only in the lattice but also in the electronic properties, including reduction of its band gap to optimize both UV and visible light absorption.

$ZnWO_4$ doped with metals ions

Many studies have been carried out on $ZnWO_4$ catalyst doped with different metal ions in order to improve the functionalities of the material. In this context, Dutta and Raval [100] reported the photocatalytic application of $ZnWO_4$ nanoparticles doped with Cr^{3+}, Mn^{2+}, and Cu^{2+} ions synthesized by a sonochemical method. Methylene blue, simulated sunlight irradiation, and 30 mg of the catalyst were used in the photodegradation tests. It was observed that all the samples, including doped and pure $ZnWO_4$, achieved 100% of MB degradation. The difference in photocatalytic behavior of the materials was related only to the time variation. Pure $ZnWO_4$ degraded MB dye solution after 150 min, while Mn^{2+}-doped $ZnWO_4$ had a reduced time of 120 min, followed by Cu^{2+}-doped $ZnWO_4$ that completely degraded MB after 90 min, and finally, Cr^{3+}-doped $ZnWO_4$ achieved the best efficiency of dye degradation after 75 min. It was also observed that Cr^{3+}-doped $ZnWO_4$ presented the lowest band gap energy (E_g=2.72 eV) among the catalysts and, consequently, the greatest efficiency in absorbing visible light. The authors attributed the photocatalytic efficiency of the doped materials to the creation of different sublevels within the band gap, which act as electron and hole traps and facilitate charge separation, enhancing photocatalytic activity. In a different work, Li^+ was also used as a dopant by Xiong et al. [101] to prepare $Zn_{1-x}WO_4$:xLi^+ catalysts by the solid-state reaction method, with variation in Li^+ concentration (x= 0, 0.02, 0.05, 0.10). The samples were applied for RhB dye degradation under UV irradiation with a catalyst/dye concentration of 0.4 mg.mL^{-1}. The authors reported that the band gap values decreased from 3.93 to 3.55 eV for pure $ZnWO_4$ and $ZnWO_4$ doped with 0.1 mol% Li^+, respectively. The authors mentioned that the addition of Li^+ provided a greater absorption capacity by inducing intermediate levels in the band gap. Thus, more electrons and photogenerated holes can be provided to improve the photocatalytic activity in the doped material. $Zn_{0.9}WO_4$:0.1Li^+ showed the best efficiency, degrading RhB by about 76.7% after 120 min. According to the authors, when Li^+ is incorporated into the host lattice, new electron traps are introduced, increasing the number of the carriers trapped by this center, and delaying electron-hole pairs recombination. Therefore, as more electrons and holes are separated, the photocatalytic activity of Li-doped $ZnWO_4$ is increased.

Pan et al. [102] synthesized $ZnWO_4$ doped with different titanium content (Ti^{4+}= 0.5, 1, and 2 mol%) by solid-state reaction method and evaluated the photocatalytic properties toward the degradation of RhB under UV light irradiation using a catalyst/dye concentration of 0.2 mg.mL^{-1}. As a result of the photocatalytic tests, the authors observed that Ti^{4+} dopants provided an increased photocatalytic activity of $ZnWO_4$ (E_g=4.12 eV) by decreasing the band gap value, reaching 97% of RhB dye degradation after 120 min when $ZnWO_4$:0.01% Ti (E_g=3.34 eV) was used as a catalyst against 86% of dye degradation when pure $ZnWO_4$ was used in the process. The authors justified the highest photocatalytic efficiency observed for Ti^{4+}-doped $ZnWO_4$ samples to the fact that doping with Ti^{4+} ions shortens the band gap and improves the photoresponse of $ZnWO_4$ material, which may lead to greater efficiency in the separation of photogenerated electron-hole pairs. Zhang et al. [103] synthesized Bi^{3+} and Cu^{2+}-doped $ZnWO_4$ samples by hydrothermal method, with a variation of Bi^{3+} and Cu^{2+} molar content at 0, 1, 2, 3, and 4 mol%. The MB dye was used to evaluate the photocatalytic activity of the materials under UV light irradiation. It was observed a proportional variation in the optical absorption band of Cu-$ZnWO_4$ as a function of the Cu^{2+} content added in the lattice and the absorption of UV light decreases dramatically as Cu^{2+} ions are introduced in the system until the absorption region changes to the visible light wavelengths. Regarding the band gap (E_g), the authors showed a decrease in E_g values from 3.30 to 2.96 eV for $ZnWO_4$ and 3%Cu-$ZnWO_4$, respectively. However, by further increasing the Cu^{2+} content to 4%, the band gap increases to 2.99 eV, indicating that there is an ideal amount of Cu^{2+} doping to optimize the band gap in order to improve the material functionality. In relation to the photocatalytic efficiency of the studied catalysts, the highest efficiency (99.4%) for 3% Cu^{2+}-$ZnWO_4$ after 90 min of irradiation followed by the 3% Bi^{3+}-$ZnWO_4$ (99%) after 2 h of irradiation was observed. The pure $ZnWO_4$ photocatalyst

presented only 78% of MB degradation. The authors also revealed that higher amounts of Bi^{3+} provided a decrease in photocatalytic activity for MB degradation, as the excess of Bi^{3+} dopant introduces new energy levels within the band gap that act as recombination centers, increasing the possibility of recombination and consequently reduction of the photocatalytic activity.

Rare earth metals, such as Eu^{3+}, Ce^{3+}, and La^{3+}, are also commonly used as dopants to improve the photocatalytic behavior of $ZnWO_4$. For instance, Dong et al. [104] synthesized $ZnWO_4$ doped with 0.5, 2, 3, 4, and 5 mol% of Eu^{3+} by surface self-propagating combustion method for the photodegradation of RhB under UV irradiation. In the photocatalytic experiments, a catalyst/dye concentration of 1 $mg.mL^{-1}$ was used. The best photocatalytic efficiency was observed for the $ZnWO_4$ sample containing 4% of Eu^{3+}. According to the authors, the difference in photocatalytic activity observed for the samples was associated with the different oxidation states on the surface of the Eu^{3+}-doped $ZnWO_4$, due to the Eu^{3+}/Zn^{2+} substitution. It was pointed out that Eu^{3+}/Zn^{2+} substitution can be compensated by the formation of cationic vacancies that can act as traps for photogenerated holes. However, the authors warned that capturing photogenerated holes can even reduce the recombination rate of photogenerated charge carriers leading to an improvement of the photocatalytic activity, but it can also reduce the amount of photogenerated holes (h^+) available for reaction, resulting in a lower photocatalytic activity as the h^+ play an important role in the direct photooxidation of the molecules or in the formation of $^{\bullet}OH$ radicals during photocatalysis. In this context, an optimal balance in the amount of Eu^{3+} doping and the creation of electronic defects is crucial for tuning the photocatalytic properties of the materials. Phuruangrat et al. [38] synthesized $ZnWO_4$ doped with Ce^{3+} ions by hydrothermal method at different Ce^{3+} molar concentrations (0, 1, 2, and 3 mol%) and employed for the photodegradation of MB dye under UV light, with a catalyst/dye concentration of 0.2 $mg.mL^{-1}$. Similar to the results reported by other authors, Phurangrat et al. [38] also showed that doping $ZnWO_4$ with Ce^{3+} provided greater photocatalytic efficiency, especially when the doping is performed using 3 mol% Ce^{3+}, degrading 99.13% of MB in 60 min. According to the authors, this efficiency is due to the formation of Ce^{4+} defects on the surface of the catalyst which act as electron traps in the CB reducing to Ce^{3+}. Therefore, Ce^{3+} ions are oxidized by electron transfer to the adsorbed O_2 molecules that produce the $O_2^{\bullet-}$ radicals, and then electron-hole pair recombination is reduced and photocatalytic activity in Ce^{3+}-doped $ZnWO_4$ improved.

Although organic dyes have been the most explored target molecules to evaluate the photocatalytic efficiency of $ZnWO_4$-doped materials, other important pollutants have also been studied. For instance, Ma et al. [105] prepared $ZnWO_4$ nanorods doped with Na in a one-step hydrothermal strategy using Na_2WO_4 as a dopant source. Na-doped $ZnWO_4$ nanorods presented a pronounced photocatalytic efficiency for benzene degradation at 50 ppm in a self-designed continuous flow reaction system. For the experiment, 0.4 g of the photocatalyst was dispensed on four glass sheets with a small amount of ethanol, dried at 60 °C, and put into the reactor, equipped with a 300 W mercury lamp as a visible light source. It was evidenced, using X-ray photoelectron spectroscopy (XPS) and electron paramagnetic resonance (EPR) measurements, that the presence of oxygen vacancies and Na element in the prepared Na-doped $ZnWO_4$ nanorods, which favored the increase in the photocatalytic efficiency of this sample toward benzene degradation. By using time-dependent *in situ* DRIFTS spectra and DFT calculations, the authors demonstrated benzene oxidation over the nanorods. In this photocatalytic degradation process, $ZnWO_4$-Na is excited to generate h^+/e^- pairs under irradiation that react with H_2O and O_2 to produce $^{\bullet}OH$ and $O_2^{\bullet-}$. On the catalytic surface, benzene molecules react with these radicals, generating the phenolate species. Since phenol is easily oxidized to produce catechol and hydroquinone, o-benzoquinone and p-benzoquinone are thus produced. Afterward, a ring-opening reaction occurs under the action of radicals to form small molecule organic compounds such as acetic acid, and finally, the small organic molecules are oxidized to form H_2O and CO_2, and the photocatalytic oxidation of benzene is completed.

In another work, Nie et al. [106] synthesized the $ZnWO_4$ nanorods doped with different concentrations of La^{3+} ions (0.4, 0.6, 0.8, and 1.2 mol%) by hydrothermal method. The prepared samples were applied in nitric oxide (NO) oxidation under simulated sunlight irradiation, using 100 mg of the catalyst. It was observed that $ZnWO_4$ doped with 0.6 mol% La^{3+} exhibited the best photocatalytic activity, reaching 46% of NO removal after 30 min. It was evidenced that the band gap energy decreased from 3.56 eV for pure $ZnWO_4$ to 3.23 eV in 0.6%La-$ZnWO_4$. The authors attributed the photocatalytic efficiency of the nanorods to the synergistic effect induced by La^{3+} doping and the creation of oxygen vacancies in the $ZnWO_4$ lattice, which enhanced charge separation during photocatalysis. It was emphasized that, although the activity of $ZnWO_4$ photocatalysts was improved by La^{3+} content, the excess of such dopant ($La^{3+} \geq 0.8\%$) promoted a decrease in photocatalytic efficiency. According to the authors, the excess amount of La^{3+} ions can act as recombination centers of the electron-hole pair, leading to a decrease in the efficiency of the photocatalyst. The photocatalytic mechanism proposed by Nie et al. [106] for NO removal is similar to that schematically shown in Fig. 12. Accordingly, the mechanism is initially based on the adsorption of NO on the photocatalyst surface in the dark. Then, electron-hole pairs are photogenerated under simulated sunlight irradiation. Photoinduced h^+ reacts with hydroxyl groups (OH^-) adsorbed on the material surface to form oxygen active species like hydroxyl $^{\bullet}OH$ radicals, which further promotes NO oxidation. Simultaneously, La^{3+}, which is responsible for creating an energy level in the $ZnWO_4$ band gap, can react with photoinduced electrons to generate unstable La^{2+} species, which rapidly release electrons to reduce adsorbed oxygen (O_2) to form superoxide $O_2^{\bullet-}$ radicals. The authors,

however, determined the positions of the VB and CB, based on the Mott-Schottky method. Furthermore, the authors report in detail, that oxygen vacancies (V_O), induced by La^{3+} doping and calculated by DFT, participate in the formation of NO_2^-/NO_3^- and in a series of other redox processes on the photocatalyst surface. As a result, La^{3+} doping and induced V_O boost the utilization of the light source as well as promote an enhanced separation of the photoinduced electron-hole pairs.

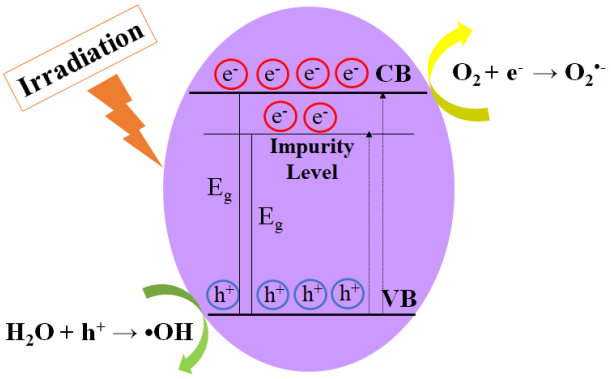

Figure 12: Hypothetical photocatalysis mechanism for a semiconductor doped with a metal cation.

$ZnWO_4$ doped with nonmetal ions

Nonmetals were not widely employed for doping $ZnWO_4$ when compared to metals, however, fluorine (F) has been the most used nonmetals dopant in this case. For instance, Huang and Zhu [107] investigated the photocatalytic properties of $ZnWO_4$ doped with various molar ratios of Zn and F (0, 0.1, 0.2, 0.4, 0.8, 1.0, and 3.0) synthesized at 180 ºC for 24 h by hydrothermal method. The photodegradation of RhB was performed under UV irradiation using a catalyst/dye concentration of 0.5 $mg.mL^{-1}$. The highest photocatalytic efficiency was achieved for the sample prepared with a 0.4 Zn/F ratio, reaching an RhB degradation of 90% after 60 min under irradiation. The authors suggested that the best photocatalytic activity observed for the 0.4 Zn/F sample was mainly due to an ideal balance in dopant and good surface area (24.8 $m^2.g^{-1}$), as the 0.1 Zn/F sample presented a similar surface area (24.7 $m^2.g^{-1}$). However, even if a larger surface area is important to adsorb the substrate, it was emphasized that control of doping is the most important factor to obtain a significant increase in photocatalytic efficiency. Another study using F as doping in $ZnWO_4$ was reported by Chen et al. [108], in which F-doped $ZnWO_4$ nanorods at 0.5 mol% were synthesized by the hydrothermal method. A photocatalytic evaluation was performed using RhB under UV irradiation with a catalyst/dye concentration of 0.5 $mg.mL^{-1}$. It was explained that F doping extends the photoresponse of $ZnWO_4$ to longer wavelength regions, which increased the number of electrons and holes photogenerated during the photocatalytic reaction. Regarding photocatalytic efficiency, different samples were investigated which were: $ZnWO_4$ nanoparticles prepared without hydrothermal treatment, $ZnWO_4$ nanorods synthesized by hydrothermal treatment at 180 °C for 12 h, F-$ZnWO_4$ nanoparticles prepared without hydrothermal treatment, and F-$ZnWO_4$ nanorods prepared by a two-step hydrothermal treatment. Among these samples, F-$ZnWO_4$ nanorods showed the best photocatalytic efficiency of 95.5% RhB degradation after only 60 min of irradiation. The authors correlated the particle morphology of F-$ZnWO_4$ samples with their photocatalytic properties, in which F-$ZnWO_4$ nanorods displayed a much higher photocatalytic efficiency because of the anisotropic growth and higher crystallinity of this sample caused by the hydrothermal treatment. Furthermore, it was suggested that the irregular nanoparticles of the F-$ZnWO_4$ sample prepared without hydrothermal treatment showed low activity due to the low crystallinity and the higher concentration of defects that may act as an electron-hole pair recombination center. The authors concluded that morphology, crystallinity, and F-doping had a great impact on tuning the photocatalytic activity of $ZnWO_4$ material.

In a recent work, Hung et al. [109] synthesized F-doped $ZnWO_4$ in a two-step process, which consists in producing an ionic powder mixture using a stoichiometric amount of $Zn(COOCH_3)$, $Na_2WO_4.2H_2O$ and NH_4F precursors, followed by annealing at 700 ºC in a tube furnace for 2 h in order to obtain crystalline powders. The molar ratios used for F were 2, 4, 6, 8, and 10 mol%, and photocatalytic properties of the powders were investigated in the degradation of the MB dye under UV irradiation. Regarding the band gap, the increase of the doping amounts up to 4 mol% of F provoked a decrease in the band gap of $ZnWO_4$ to 3.20 eV, increasing for higher concentrations of F. The authors suggested that the decrease in the band gap observed in the F-doping molar range of 0-4 mol% is associated with the presence of F at interstitial sites in the $ZnWO_4$ crystal lattice. Regarding photocatalytic activity, it was observed the highest photocatalytic activity for the $ZnWO_4$ sample doped with 4% of F concentration, reaching 85% of MB degradation after 5 h. The best photocatalytic efficiency attained with this sample was attributed to some important parameters, such as: morphology, as the increase in the specific surface area of the synthesized nanorods and nanowires increased dye adsorption leading to a faster rate of photodegradation; the decrease in the number of defects, especially those ones related to hydrogen, which may act as recombination centers for electron-hole pairs; and the decrease in band gap energy that results in an increase in photoresponse at different irradiation wavelength.

In addition to F, other nonmetals were used for doping $ZnWO_4$, such as nitrogen, as reported by Sethi et al. [110] who synthesized N-doped $ZnWO_4$ nanorods by hydrothermal method followed by heat treatment in the presence of thiourea (TU) to promote nitrogen doping. The ratio of $ZnWO_4$:TU was varied at 1:1, 1:2, and 1:3. The photocatalytic behavior of the nanorods was investigated in the degradation of RhB dye under direct sunlight irradiation. It was observed that

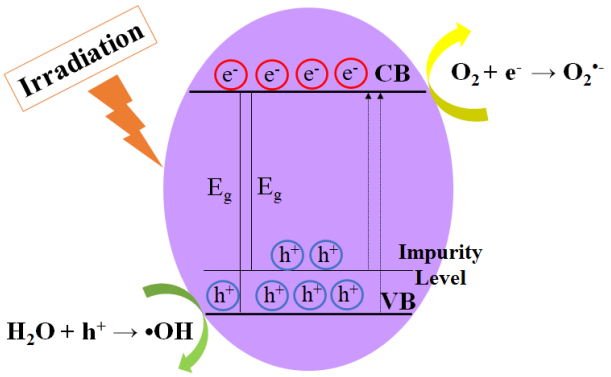

Figure 13: Hypothetical photocatalysis mechanism for a doped semiconductor.

the band gap of pure $ZnWO_4$ (3.48 eV) decreased to 3.42, 2.68, and 2.52 eV after N incorporation by $ZnWO_4$:TU ratio variation at 1:1, 1:2, and 1:3, respectively. As expected for N-doped materials, a significant increase in the visible light absorption was observed, due to electronic changes caused by the presence of nitrogen in the tungstate lattice, which was demonstrated by DFT simulations. The highest photocatalytic efficiency was evidenced for the N-$ZnWO_4$ sample prepared in a higher TU concentration, providing a complete degradation of the RhB dye after 120 min. The authors pointed out that the increase in photocatalytic activity was mainly attributed to nitrogen doping and justified by the increase of the surface area from 9.0 to 13.61 $m^2.g^{-1}$ after nitrogen doping.

The mechanism used for doping $ZnWO_4$ with both metals and nonmetals is very similar and can be seen in Fig. 13. In the case shown in Fig. 13, the mechanism is initially based on the adsorption of the pollutant on the surface of the photocatalyst and, after irradiation, the electron-hole pairs are photogenerated. The photoinduced h^+ reacts with the hydroxyl groups (OH^-) adsorbed on the surface of the material to form active species such as $^{\bullet}OH$. Simultaneously, the impurity used in doping is responsible for creating an energy level in the band gap of $ZnWO_4$, which can react with photoinduced electrons to generate unstable ion species, which rapidly release electrons to reduce the adsorbed oxygen to form $O_2^{\bullet-}$ radicals. Both $^{\bullet}OH$ and $O_2^{\bullet-}$ radicals also promote the oxidation and reduction of the organic pollutant [106]. Table III summarizes important works concerning doped $ZnWO_4$ material applied in the photodegradation of different contaminants.

CONCLUSIONS

Our review research concerning $ZnWO_4$ has demonstrated that this tungstate can be considered a versatile and important material used for applications in different photocatalytic processes such as degradation, mineralization, oxidation, and reduction of a variety of pollutants. Among them, the photodegradation of organic contaminants such as dyes, pharmaceuticals, phenols, formaldehyde, and toluene,

Table III - $ZnWO_4$ doped with different ions applied in the photodegradation of organic pollutants.

Catalyst type	Synthesis method	Catalyst concentration (mg)	Pollutant	Light source	Efficiency (%)	Time (min)
$ZnWO_4$:Co^{2+} [111]	Hydrothermal	1.0	RhB; MB; MO; Cr(VI)	UV	94.4[a]/97.8[b] (RhB); 95 (MB); 86.4 (MO); 99 [Cr(VI)]	120
$ZnWO_4$:F [108]	Hydrothermal	0.5	RhB	UV	95.5	60
$ZnWO_4$:Dy^{3+}, Bi^{3+} [112]	Solid-state reaction	0.4	RhB	UV	99.9	40
$ZnWO_4$:Eu^{3+} [104]	Combustion	1.0	RhB	UV	~95	100
$ZnWO_4$:F [113]	Hydrothermal	0.5	4-CP	UV	99	180
$ZnWO_4$:F [107]	Hydrothermal	0.5	RhB	UV	90	60
$ZnWO_4$:N [110]	Hydrothermal + heat treatment with urea	-	RhB	Direct sunlight	100	120
$ZnWO_4$:Bi^{3+} [99]	Two-step hydrothermal-solvothermal	-	NO	Visible; simulated sunlight	1.91 (visible); 45.87 (simulated sunlight)	30
$ZnWO_4$:Dy^{3+} [114]	Hydrothermal	0.5	MB	UV	97.46	60
$ZnWO_4$:Ce [38]	Hydrothermal	0.5	MB	UV	99.13	60
$ZnWO_4$:Cd [115]	Hydrothermal	0.3	RhB	UV	100	30
$ZnWO_4$:Sn^{2+} [116]	Microwave-assisted hydrothermal	0.5	MO	Visible	~90	160

RhB: rhodamine B; MB: methylene blue; MO: methyl orange; 4-CP: 4-chlorophenol; NO: nitric oxide; [a]: degradation; [b]: oxidation.

besides inorganic contaminants such as nitric oxide (NO), chromium(VI), and vanadium(V) elements has been achieved by different authors using $ZnWO_4$-based catalysts either under UV-visible light or simulated sunlight irradiation. It has been shown that strategies like the formation of heterojunctions with various other semiconductors and doping with different metal and nonmetal ions provide a remarkable improvement in the photocatalytic performance of $ZnWO_4$ as compared to its pure form. For pure $ZnWO_4$, synthesis conditions may influence particle morphology, surface area, crystallinity, and electronic defects, which are important parameters to modify photocatalytic activity. In doped $ZnWO_4$ catalysts, metals and nonmetals dopants may introduce intermediate levels decreasing the band gap, so an improvement of the photoresponse in UV-visible light has been reported for different dopants. On the other hand, it has been demonstrated that the formation of heterostructures of $ZnWO_4$ with other materials is responsible for band structure alignment and improvement of the photocatalytic activity by retarding the time for charge carrier recombination. Despite presetting great photostability, evaluation of the works concerning $ZnWO_4$ showed an absence of detailed information about the mechanism and photodegradation pathways of organic pollutants and the formation of by-products. In addition to that, the type of exposed surface is a key factor that defines the photoactivity of $ZnWO_4$, which impact significantly on the redox ability of photoinduced carriers. All these data show that deep knowledge about the surface chemical engineering strategy by crystal or thin film growth may be necessary to pave a new pathway to obtain other $ZnWO_4$-based materials for photocatalysis application.

ACKNOWLEDGEMENTS

The authors acknowledge CNPq/MCTIC, PRONEX/FAPESQ/CNPq (Edital FAPESQ), and CAPES (finance code 001) for the financial support. A.L.M.O. thanks CAPES for the PNPD fellowship (Grant 88882.317938/2019-01).

REFERENCES

[1] C.C.A. Loures, M.A.K. Alcântara, H.J.I. Filho, A.C.S.C. Teixeira, F.T. Silva, T.C.B. Paiva, G.R.L. Int. Rev. Chem. Eng. **5** (2013) 102.
[2] N.N. De Brito, G. Archanjo Brota, R. Teixeira Pelegrini, J.E. Stipp Paterniani, Eclética Quím. J. **36** (2017) 1.
[3] R. Andreozzi, V. Caprio, A. Insola, R. Marotta, Catal. Today **53** (1999) 51.
[4] C.C. de Amorim, M.M.D. Leão, R.F.P.M. Moreira, Eng. Sanit. Amb. **14** (2009) 543.
[5] K.S. de Araújo, R. Antonelli, B. Gaydeczka, A.C. Granato, G.R.P. Malpass, Rev. Amb. Água **11** (2016) 387.
[6] T.N.M. Cervantes, D.A.M. Zaia, H. de Santana, Quim. Nova **32** (2009) 2423.
[7] R.F.P. Nogueira, W.F. Jardim, Quim. Nova **21** (1998) 69.
[8] R. Ameta, M.S. Solanki, S. Benjamin, S.C. Ameta, J.R.N.R. Vidyapeeth, in "Adv. oxid. process waste water treat.", S.C. Ameta, R. Ameta (Eds.), Elsevier (2018) 135.
[9] H. Wang, L. Zhang, Z. Chen, J. Hu, S. Li, Z. Wang, J. Liu, X. Wang, R. Soc. Chem. **43** (2014) 5234.
[10] A.Y. Shan, T.I.M. Ghazi, S.A. Rashid, Appl. Catal. A Gen. **389** (2010) 1.
[11] B. Bakbolat, C. Daulbayev, F. Sultanov, R. Beissenov, A. Umirzakov, A. Mereke, A. Bekbaev, I. Chuprakov, Nanomaterials **10** (2020) 1790.
[12] V. Dutta, S. Sharma, P. Raizada, V.K. Thakur, A.A.P. Khan, V. Saini, A.M. Asiri, P. Singh, J. Environ. Chem. Eng. **9** (2021) 105018.
[13] C. Sun, J. Yang, M. Xu, Y. Cui, W. Ren, J. Zhang, H. Zhao, B. Liang, Chem. Eng. J. **427** (2022) 131564.
[14] Z. Mirzaeifard, Z. Shariatinia, M. Jourshabani, S.M. Rezaei Darvishi, Ind. Eng. Chem. Res. **59** (2020) 15894.
[15] N. Saito, H. Kadowaki, H. Kobayashi, K. Ikarashi, H. Nishiyama, Y. Inoue, Chem. Lett. **33** (2004) 1452.
[16] M.J.S. Mohamed, D.K. Bhat, AIMS Mater. Sci. **4** (2017) 158.
[17] F. Wang, W. Li, S. Gu, H. Li, X. Liu, M. Wang, ACS Sustain. Chem. Eng. **4** (2016) 6288.
[18] R. Lacomba-Perales, J. Ruiz-Fuertes, D. Errandonea, D. Martínez-García, EPL **83** (2008) 37002.
[19] L.J. Brillson, *An essential guide to electronic material surfaces and interfaces*, John Wiley Sons (2016) 223.
[20] J. Low, J. Yu, M. Jaroniec, S. Wageh, A.A. Al-Ghamdi, J.X. Low, J.G. Yu, S. Wageh, A.A. Al-Ghamdi, M. Jaroniec, Adv. Mater. **29** (2017) 1601694.
[21] R.T. Bueno, O.F. Lopes, K.T.G. Carvalho, C. Ribeiro, H.A.J.L. Mourão, Quim. Nova **42** (2019) 661.
[22] Z. Zhao, H. An, J. Lin, M. Feng, V. Murugadoss, T. Ding, H. Liu, Q. Shao, X. Mai, N. Wang, H. Gu, S. Angaiah, Z. Guo, Chem. Rec. **19** (2019) 873.
[23] Z. Zhao, B. Zhang, D. Chen, Z. Guo, Z. Peng, J. Nanosci. Nanotechnol. **16** (2016) 2847.
[24] W.G. Oldham, A.G. Milnes, Solid-State Electron. **6** (1963) 121.
[25] F.C. Marques, A.M. Stumbo, M.C. Canela, Quim. Nova **40** (2017) 561.
[26] Q. Xu, L. Zhang, J. Yu, S. Wageh, A.A. Al-Ghamdi, M. Jaroniec, Mater. Today **21** (2018) 1042.
[27] Y. Wang, D. Chen, Y. Hu, L. Qin, J. Liang, X. Sun, Y. Huang, Energy Fuels **4** (2020) 1681.
[28] P. Raizada, A. Kumar, P. Singh, Curr. Anal. Chem. **17** (2021) 150.
[29] P. Zhou, J. Yu, M. Jaroniec, Adv. Mater. **26** (2014) 4920.
[30] Q. Xu, L. Zhang, B. Cheng, J. Fan, J. Yu, Chem **6** (2020) 1543.
[31] J. Low, C. Jiang, B. Cheng, S. Wageh, A.A. Al-Ghamdi, J. Yu, Small Methods **1** (2017) 1700080.
[32] S. Bai, N. Zhang, C. Gao, Y. Xiong, Nano Energy **53** (2018) 296.
[33] H. Liu, J. Huang, J. Chen, J. Zhong, J. Li, R. Duan, Solid State Sci. **95** (2019) 105923.
[34] W.D. Callister, D.G. Rethwisch, *Ciência e engenharia de materiais: uma introdução*, 9th ed., LTC (2016).
[35] A.L.M. de Oliveira, J.M. Ferreira, M.R.S. Silva, S.C. de

Souza, F.T.G. Vieira, E. Longo, A.G. Souza, I.M.G. Santos, Dye Pigment **77** (2008) 210.
[36] A.L.M. de Oliveira, J.M. Ferreira, M.R.S. Silva, S.C. de Souza, F.T.G. Vieira, E. Longo, A.G. Souza, I.M.G. Santos, J. Therm. Anal. Calorim. **97** (2009) 167.
[37] G. Huang, C. Zhang, Y. Zhu, J. Alloys Compd. **432** (2007) 269.
[38] A. Phuruangrat, P. Dumrongrojthanath, T. Thongtem, S. Thongtem, J. Ceram. Soc. Japan **125** (2017) 62.
[39] E.C. Severo, E.R. Abaide, C.G. Anchieta, V.S. Foletto, C.T. Weber, T.B. Garlet, G.C. Collazzo, M.A. Mazutti, A. Gündel, R.C. Kuhn, E.L. Foletto, Mater. Res. **19** (2016) 781.
[40] P.F.S. Pereira, A.F. Gouveia, M. Assis, R.C. Oliveira, I.M. Pinatti, M. Penha, R.F. Gonçalves, L. Gracia, J. Andrés, R.C. de Oliveira, E. Longo, Phys. Chem. Chem. Phys. **20** (2018) 1923.
[41] D. Santamaria-Perez, D. Errandonea, P. Rodriguez-Hernandez, A. Muñoz, R. Lacomba-Perales, A. Polian, Y. Meng, Inorg. Chem. **55** (2016) 10406.
[42] R. Alvarez-Roca, A.F. Gouveia, C.C. de Foggi, P.S. Lemos, L. Gracia, L.F. da Silva, C.E. Vergani, M. San-Miguel, E. Longo, J. Andrés, Inorg. Chem. **60** (2021) 1062.
[43] S. Caubergh, N. Matsubara, F. Damay, A. Maignan, F. Fauth, P. Manuel, D.D. Khalyavin, B. Vertruyen, C. Martin, Inorg. Chem. **59** (2020) 9798.
[44] A.F. Gouveia, M. Assis, L.S. Cavalcante, E. Longo, J. Andrés, Front. Res. Today **1** (2018) 1005.
[45] G.V. Geetha, R. Sivakumar, C. Sanjeeviraja, V. Ganesh, J. Sol-Gel Sci. Technol. **97** (2021) 572.
[46] Y. Wu, S.-C. Zhang, L.-W. Zhang, Y.-F. Zhu, Chem. Res. Chin. Univ. **23**, 4 (2007) 465.
[47] M. Rahmani, T. Sedaghat, Polym. Mater. **29**, 1 (2018) 220.
[48] H. Eranjaneya, G.T. Chandrappa, Trans. Indian Ceram. Soc. **75**, 2 (2016) 133.
[49] M. Li, Q. Meng, S. Li, F. Li, Q. Zhu, B.-N. Kim, J.-G. Li, Ceram. Int. **45** (2019) 10746.
[50] J. Yan, Y. Shen, F. Li, T. Li, Sci. World J. **2013** (2013) 458106.
[51] N.F.A. Neto, T.B.O. Nunes, M. Li, E. Longo, M.R.D. Bomio, F.V. Motta, Ceram. Int. **46**, 2 (2020) 1766.
[52] Q. Wu, X. Liu, S. Hou, L. Qiang, K. Zhang, Z. Yang, Colloids Surf. A Physicochem. Eng. Asp. **629** (2021) 127459.
[53] K.M. Garadkar, L.A. Ghule, K.B. Sapnar, S.D. Dhole, Mater. Res. Bull. **48** (2013) 1105.
[54] S.M. Hosseinpour-Mashkani, M. Maddahfar, A. Sobhani-Nasab, J. Electron. Mater. **45** (2016) 3612.
[55] I. Altinsoy, N. Guy, M. Ozacar, C. Bindal, Arab. J. Sci. Eng. **46** (2021) 463.
[56] N.S. Pavithra, G. Nagaraju, S.B. Patil, Ionics **27** (2021) 3533.
[57] F. Su, P. Li, J. Huang, M. Gu, Z. Liu, Y. Xu, Sci. Rep. **11** (2021) 85.
[58] R.A.C. Amoresi, R.C. Oliveira, N.L. Marana, P.B. De Almeida, P.S. Prata, M.A. Zaghete, E. Longo, J.R. Sambrano, A.Z. Simões, Mater. Interfaces **2** (2019) 6513.
[59] G.S. Kamble, Y.-C. Ling, Sci. Rep. **10** (2020) 12993.
[60] A.R.F.A. Teixeira, A.M. Neris, E. Longo, J.R. de Carvalho Filho, A. Hakki, D. Macphee, I.M.G. dos Santos, J. Photochem. Photobiol. A Chem. **369** (2019) 181.
[61] L.M.C. Honorio, A.L.M. de Oliveira, E.C. da Silva Filho, J.A. Osajima, A. Hakki, D.E. Macphee, I.M.G. dos Santos, Appl. Surf. Sci. **528** (2020) 146991.
[62] X. Zheng, J. Yuan, J. Shen, J. Liang, J. Che, B. Tang, G. He, H. Chen, J. Mater. Sci. Mater. Electron. **30** (2019) 5986.
[63] T. Liu, L. Wang, X. Lu, J. Fan, X. Cai, B. Gao, R. Miao, J. Wang, Y. Lv, RSC Adv. **7** (2017) 12292.
[64] G.V. Geetha, S.P. Keerthana, K. Madhuri, R. Sivakumar, Inorg. Chem. Commun. **132** (2021) 1387.
[65] V. Faka, S. Tsoumachidou, M. Moschogiannaki, G. Kiriakidis, I. Poulios, V. Binas, J. Photochem. Photobiol. A Chem. **406** (2021) 113002.
[66] S. Lin, J. Chen, X. Weng, L. Yang, X. Chen, Mater. Res. Bull. **44** (2009) 1102.
[67] Z. Luo, D. Xu, S. Zhang, J. Shen, J. Nanosci. Nanotechnol. **18** (2018) 7241.
[68] Z. Sheng, A.D. Ma, Q. He, K. Wu, L. Yang, Catal. Sci. Technol. **9** (2019) 5692.
[69] D. Sivaganesh, S. Saravanakumar, V. Sivakumar, R. Rajajeyaganthan, M. Arunpandian, J.N. Gopal, T.K. Thirumalaisamy, Mater. Charact. **159** (2020) 110035.
[70] L. Hao, H. Huang, Y. Zhang, T. Ma, Adv. Funct. Mater. **31** (2021) 2100919.
[71] M.I. Osotsi, D.K. Macharia, B. Zhu, Z. Wang, X. Shen, Z. Liu, L. Zhang, Z. Chen, Prog. Nat. Sci. Mater. Int. **28** (2018) 408.
[72] C.B. Anucha, I. Altin, Z. Biyiklioglu, E. Bacaksiz, I. Polat, V.N. Stathopoulos, Nanomaterials **10** (2020) 2139.
[73] Y. Hao, L. Zhang, Y. Zhang, L. Zhao, B. Zhang, RSC Adv. **7** (2017) 26179.
[74] C. Jaramillo-Páez, J.A. Navío, F. Puga, M.C. Hidalgo, J. Photochem. Photobiol. A Chem. **404** (2021) 112962.
[75] V. Kale, Y.M. Hunge, S.A. Kamble, M. Deshmukh, S.V. Bhoraskar, V.L. Mathe, Mater. Today Commun. **26** (2021) 102101.
[76] D.P. Ojha, H.J. Kim, Chem. Eng. Sci. **212** (2020) 115338.
[77] K.T.G. Carvalho, O.F. Lopes, C. Ferreira, C. Ribeiro, J. Alloys Compd. **797** (2019) 1299.
[78] D. He, L. Wang, D. Xu, J. Zhai, D. Wang, T. Xie, ACS Appl. Mater. Interfaces **3** (2011) 3167.
[79] P. Kumar, S. Verma, N.Č. Korošin, B. Žener, U.L. Štangar, Catal. Today **397-399** (2022) 278.
[80] Z. Li, X. Liu, N. Bai, Q. Wu, K. Zhang, J. Mater. Sci. Mater. Electron. **32** (2021) 14456.
[81] P. Dumrongrojthanath, A. Phuruangrat, S. Thongtem, T. Thongtem, Rare Met. **38** (2019) 601.
[82] M. Li, Q. Zhu, J.-G. Li, B.-N. Kim, Appl. Surf. Sci. **515** (2020) 146011.
[83] P. Huo, Y. Tang, M. Zhou, J. Li, Z. Ye, C. Ma, L. Yu, Y. Yan, J. Ind. Eng. Chem. **37** (2016) 340.
[84] Q. Wang, Y. Shi, T. Niu, J. He, H. She, B. Su, J. Sol-Gel Sci. Technol. **83** (2017) 555.

[85] N. Alhokbany, S.M. Alshehri, J. Ahmed, Catalysts **11** (2021) 1536.
[86] C.V. Reddy, R. Koutavarapu, K.R. Reddy, N.P. Shetti, T.M. Aminabhavi, J. Shim, J. Environ. Manage. **268** (2020) 110677.
[87] X. Shan, T. Jia, F. Fu, Catalysts **11** (2021) 1345.
[88] A. Hamrouni, N. Moussa, A. Di Paola, L. Palmisano, A. Houas, F. Parrino, J. Photochem. Photobiol. A Chem. **309** (2015) 47.
[89] S. Gong, G. Zhu, I.A. Bello, F. Rao, S. Li, J. Gao, S.M. Zubairu, J. Peng, M. Hojamberdiev, J. Chem. Technol. Biotechnol. **95** (2020) 1705.
[90] V. Rathi, A. Panneerselvam, R. Sathiyapriya, Diam. Relat. Mater. **108** (2020) 107981.
[91] X.C. Song, W.T. Li, W.Z. Huang, H. Zhou, Y.F. Zheng, H.Y. Yin, Mater. Chem. Phys. **160** (2015) 251.
[92] L. Sun, X. Zhao, C.J. Jia, Y. Zhou, X. Cheng, P. Li, L. Liu, W. Fan, J. Mater. Chem. **22** (2012) 23428.
[93] N. Tian, H. Huang, Y. Zhang, Y. He, J. Mater. Res. **29** (2014) 641.
[94] L. Tian, Y. Rui, K. Sun, W. Cui, Nanomaterials **8** (2018) 33.
[95] F. Wang, W. Li, S. Gu, H. Li, H. Zhou, X. Wu, RSC Adv. **5** (2015) 89940.
[96] X.J. Wen, C.-H. Shen, Z.-H. Fei, C.-G. Niu, Q. Lu, J. Guo, H.-M. Lu, Colloids Surf. A Physicochem. Eng. Asp. **573** (2019) 137.
[97] Y. Wu, J. Tie, C. Chen, N. Luo, D. Yang, W. Hu, X. Liu, Ceram. Int. **45** (2019) 13656.
[98] Z. Zhang, S. Shao, J. Dang, C. Lu, W. Guan, F. Qin, Water Sci. Technol. **77** (2018) 1204.
[99] S. Li, L. Chang, J. Peng, J. Gao, J. Lu, F. Zhang, G. Zhu, M. Hojamberdiev, J. Alloys Compd. **818** (2020) 152837.
[100] D.P. Dutta, P. Raval, J. Photochem. Photobiol. A Chem. **357** (2018) 193.
[101] G.T. Xiong, W. Zhang, Z.F. Hu, P.J. Hu, Y.M. Pan, Z.Y. Feng, L. Ma, Y.H. Wang, L. Luo, J. Lumin. **206** (2019) 370.
[102] Y.M. Pan, W. Zhang, Z.F. Hu, Z.Y. Feng, L. Ma, D.P. Xiong, P.J. Hu, Y.H. Wang, H.Y. Wu, L. Luo, J. Lumin. **206** (2019) 267.
[103] K. Zhang, X. Liu, S. Hou, L. Qiang, Q. Wu, Z. Yang, J. Mater. Sci. Mater. Electron. **33**, 1 (2021) 406.
[104] T. Dong, Z. Li, Z. Ding, L. Wu, X. Wang, X. Fu, Mater. Res. Bull. **43** (2008) 1694.
[105] D. Ma, L. Yang, Z. Sheng, Y. Chen, Chem. Eng. J. **405** (2021) 126538.
[106] J. Nie, Q.U. Hassan, Y. Jia, J. Gao, J. Peng, J. Lu, F. Zhang, G. Zhu, Q. Wang, Inorg. Chem. Front. **7** (2020) 356.
[107] G. Huang, Y. Zhu, J. Phys. Chem. C **111** (2007) 11952.
[108] S. Chen, S. Sun, H. Sun, W. Fan, X. Zhao, X. Sun, J. Phys. Chem. C **114** (2010) 7680.
[109] N.M. Hung, L.T.M. Oanh, D.D. Bich, N.D. Lai, N.T. Thao, D.T.X. Thao, Mater. Trans. **58**, 9 (2017) 1245.
[110] Y.A. Sethi, C.S. Praveen, R.P. Panmand, A. Ambalkar, A.K. Kulkarni, S.W. Gosavi, M.V. Kulkarni, B.B. Kale, Catal. Sci. Technol. **8** (2018) 2909.
[111] U. Alam, A. Khan, D. Bahnemann, M. Muneer, J. Environ. Chem. Eng. **6** (2018) 4885.
[112] S. Deng, W. Zhang, Z. Hu, Z. Feng, P. Hu, H. Wu, L. Ma, Y. Pan, Y. Zhu, G. Xiong, Appl. Phys. A **124** (2018) 526.
[113] G. Huang, S. Zhang, T. Xu, Y. Zhu, Environ. Sci. Technol. **42** (2008) 8516.
[114] A. Phuruangrat, P. Dumrongrojthanath, S. Thongtem, T. Thongtem, Mater. Lett. **166** (2016) 183.
[115] X.C. Song, Y.F. Zheng, E. Yang, G. Liu, Y. Zhang, H.F. Chen, Y.Y. Zhang, J. Hazard. Mater. **179** (2010) 1122.
[116] Y. Su, B. Zhu, K. Guan, S. Gao, L. Lv, C. Du, L. Peng, L. Hou, X. Wang, J. Phys. Chem. C **116** (2012) 18508.
(Rec. 09/10/2021, Rev. 04/02/2022, 06/04/2022, Ac. 10/05/2022)